

Investigating Emission Line Galaxy Surveys with the Sloan Digital Sky Survey Infrastructure

Johan Comparat,¹ Jean-Paul Kneib,¹ Stephanie Escoffier,² Julien Zoubian,¹ Anne Ealet,² Fabrice Lamareille,^{3,4} N. Mostek,⁵ Oliver Steele,⁶ Eric Aubourg,¹³ Stephen Bailey,⁵ Adam S. Bolton,¹² Joel Brownstein,⁸ Kyle Dawson,⁵ Jian Ge,¹⁴ Olivier Ilbert,¹ Alexie Leauthaud,⁷ Claudia Maraston,⁶ Will Percival,⁶ Nicholas P. Ross,⁵ Carlo Schimd,¹ David J. Schlegel,⁵ Donald P. Schneider,^{9,10} Daniel Thomas,⁶ Jeremy L. Tinker,¹¹ Benjamin A. Weaver¹¹

¹Aix Marseille Université, CNRS, LAM (Laboratoire d'Astrophysique de Marseille) UMR 7326, 13388, Marseille, France

²Centre de Physique des Particules de Marseille, Université d'Aix-Marseille, CNRS/IN2P3, Marseille, France

³Université de Toulouse; UPS-OMP; IRAP; Toulouse, France

⁴CNRS; IRAP; 14, avenue Edouard Belin, F-31400 Toulouse, France

⁵Lawrence Berkeley National Laboratory, One Cyclotron Road, Berkeley, CA 94720

⁶Institute of Cosmology and Gravitation (ICG), Dennis Sciama Building, Burnaby Road, Univ. of Portsmouth, Portsmouth, PO1 3FX, UK

⁷Institute for the Physics and Mathematics of the universe (IPMU), The University of Tokyo, Chiba 277-8582, Japan

⁸Department of Physics and Astronomy, University of Utah, Salt Lake City, UT 84112, USA

⁹Department of Astronomy and Astrophysics, The Pennsylvania State University, University Park, PA 16802

¹⁰Institute for Gravitation and the Cosmos, The Pennsylvania State University, University Park, PA 16802

¹¹Center for Cosmology and Particle Physics, New York University, New York, NY 10003 USA

¹²Department of Physics and Astronomy, University of Utah, 115 South 1400 East, Salt Lake City, UT 84112, USA

¹³APC, Univ. Paris Diderot, CNRS/IN2P3, CEA/Irfu, Obs de Paris, Sorbonne Paris Cité, France

¹⁴Department of Astronomy, University of Florida, USA.

Accepted October 2nd 2012 by MNRAS. Received in original form July 17th 2012.

ABSTRACT

The Baryon Acoustic Oscillation (BAO) feature in the power spectrum of galaxies provides a standard ruler to probe the accelerated expansion of the Universe. The current surveys covering a comoving volume sufficient to unveil the BAO scale are limited to redshift $z \lesssim 0.7$. In this paper, we study several galaxy selection schemes aiming at building an emission-line-galaxy (ELG) sample in the redshift range $0.6 < z < 1.7$, that would be suitable for future BAO studies using the Baryonic Oscillation Spectroscopic Survey (BOSS) spectrograph on the Sloan Digital Sky Survey (SDSS) telescope. We explore two different colour selections using both the SDSS and the Canada France Hawaii Telescope Legacy Survey (CFHT-LS) photometry in the u , g , r , and i bands and evaluate their performance selecting luminous ELG. From about 2,000 ELG, we identified a selection scheme that has a 75 percent redshift measurement efficiency. This result confirms the feasibility of massive ELG surveys using the BOSS spectrograph on the SDSS telescope for a BAO detection at redshift $z \sim 1$, in particular the proposed *eBOSS* experiment, which plans to use the SDSS telescope to combine the use of the BAO ruler with redshift space distortions using emission line galaxies and quasars in the redshift $0.6 < z < 2.2$.

Key words: cosmology - large scale structure - galaxy - selection - baryonic acoustic oscillations

1 INTRODUCTION

With the discovery of the acceleration of the expansion of the universe (Riess et al. 1998; Perlmutter et al. 1999), possibly driven by a new form of energy with sufficient negative pressure, recent results have concluded that ~ 96 percent of the energy density of the uni-

verse is in a form not conceived by the Standard Model of particle physics and not interacting with the photons, hence dubbed “dark”. Lying at the heart of this discovery is the distance-redshift relation mapped by the type Ia supernovae (SNIa) combined with the temperature power spectrum of the cosmic microwave background

Table 1. Requirements for measuring at 1 percent the BAO signal. \bar{n} is the required density to overcome shot noise. The observed density [galaxy deg^{-2}] is the projection of \bar{n} on the sky. The Sample variance area required [deg^2] corresponds to the area necessary to obtain an effective volume of $1 \text{ Gpc}^3 h^{-3}$ at $k_1 \simeq 0.063 h \text{ Mpc}^{-1}$ and $k_2 \simeq 0.12 h \text{ Mpc}^{-1}$ given the value \bar{n} . N_{req} is the number of thousands of redshifts required to detect BAO at k_1 and k_2 : it is the product of the required observed density multiplied by the area required. ‘req.’ stands for required.

redshift range	Shot Noise req.		observed density req.		Sample variance area req. [deg^2]	N_{req} [10^3 redshifts]	
	$\bar{n}(k_1)$ $10^{-4} h^3 \text{Mpc}^{-3}$	$\bar{n}(k_2)$	for k_1	for k_2		for k_1	for k_2
[0.3, 0.6]	1.0	2.1	33	71	6188	204	440
[0.6, 0.9]	1.1	2.5	75	162	2585	194	419
[0.9, 1.2]	1.3	2.9	121	261	1615	195	421
[1.2, 1.5]	1.5	3.2	164	354	1227	201	435
[1.5, 1.8]	1.7	3.6	273	589	1041	284	613

fluctuations. Since the first detections, there has been a huge increment of data up to redshift $z \sim 1$ (Riess et al. 1998, Perlmutter et al. 1999, Astier et al. 2006, Wood-Vasey et al. 2007, Riess et al. 2004, Riess et al. 2007, Dawson et al. 2009; Riess et al. 2011). The current precision and accuracy required to obtain deeper insight on the cosmological model using SNIa is limited by the systematic errors of this probe; therefore a joint statistical analysis with other probes is mandatory to assess a firm picture of the cosmological model.

Corresponding to the size of the well-established sound horizon in the primeval baryon-photon plasma before photon decoupling (Peebles & Yu 1970), the BAO scale provides a standard ruler allowing for geometric probes of the global metric of the universe. In the late-time universe it manifests itself in an excess of galaxies with respect to an unclustered (Poisson) distribution at the comoving scale $r \sim 100 h^{-1} \text{Mpc}$ — corresponding to a fundamental wave mode $k \sim 0.063 h \text{Mpc}^{-1}$. The value of this scale at higher redshift is accurately measured by the peaks in the CMB power spectrum (e.g. Komatsu et al. 2009, 2011). Galaxy clustering and CMB observations therefore allow for a consistent comparison of the same physical scale at different epochs.

The first detection of the ‘local’ BAO (Cole et al. 2005; Eisenstein et al. 2005) were based on samples at low redshift $z \leq 0.4$. Further analysis on a larger redshift range ($z > 0.5$) and a wider area confirm the first result, reducing the errors by a factor of 2 (Percival et al. 2010; Blake et al. 2011). Measurements of the BAO feature have thus become an important motivation for large galaxy redshift surveys; the small amplitude of the baryon acoustic peak, and the large value of r_{BAO} , require comoving volumes of order of $\sim 1 \text{Gpc}^3 h^{-3}$ and at least 10^3 galaxies to ensure a robust detection (e.g. Tegmark 1997a; Blake & Glazebrook 2003).

BAO studies using luminous red galaxies (LRG) are currently being pushed to $z = 0.7$ by the Baryonic Oscillation Spectroscopic Survey (BOSS) experiment as part of the Sloan Digital Sky Survey III (SDSS-III) survey (Eisenstein et al. 2011). So far, with a third of the spectroscopic data, the BAO feature has been measured at $z = 0.57$ with a 6.7σ significance (Anderson et al. 2012). The final data set, which will be completed by mid-2014, will have a mean galaxy density of about 150 galaxies per square degree over $10,000 \text{ deg}^2$. Recently, the WiggleZ experiment has obtained a significant $\sim 4.9\sigma$ detection of the BAO peak at $z = 0.6$, by combining information from three independent galaxy surveys: the SDSS, the 6-degree Field Galaxy Survey (6dFGS) and the WiggleZ Dark Energy Survey (Blake et al. 2011). In contrast to SDSS, WiggleZ has mapped the less biased, more abundant emission line galaxies (Drinkwater et al. 2010).

The next generation of cosmological spectroscopic surveys

plans to map the high-redshift universe in the redshift range $0.6 \leq z \leq 2$ using the largest possible volume; see BigBOSS (Schlegel et al. 2011), PFS-SuMIRe¹, and EUCLID². To achieve this goal, suitable tracers covering this redshift range are needed. Above $z \sim 0.6$ the number density of LRGs decreases while the bulk of galaxy population is composed of star forming galaxies (Abraham et al. 1996; Ilbert et al. 2006); it is therefore compelling to build a large sample of such type of galaxies, which allows one to cover a large area and hence a large volume. The main challenges for future BAO surveys is to efficiently select targets for which a secure redshift can be measured within a short exposure time. Contrary to continuum-based LRG survey, the observational strategy of next generation surveys such as BigBOSS, PFS-SuMIRe, and EUCLID is based on redshift measurements using emission lines, which are a common feature of star-forming galaxies. In this paper we focus on targeting strategies for selecting luminous ELGs at $0.6 < z < 1.7$ using optical photometry, and we test our strategies using the BOSS spectrograph on the SDSS telescope (Gunn et al. 2006).

The plan of the paper is as follow. In section 2, we derive the necessary ELG redshift distribution to detect the BAO feature. In section 3 we explain how the ELG selection criteria were designed using different photometric catalogs, based on the performances of the BOSS spectrograph. In section 4 we compare observed spectra issued from this selection with simulations and we discuss the efficiency of the proposed selection schemes. In section 5 we discuss the main physical properties of the ELGs. In section 6, we present the redshift distribution of the observed ELGs and how to improve the selection. In appendix A we display a representative set of the spectra observed.

Throughout this study we assume a flat ΛCDM cosmology characterized by $(\Omega_m, n_s, \sigma_8) = (0.27, 0.96, 0.81)$. Magnitudes are given in the AB system.

2 BARYON ACOUSTIC OSCILLATIONS

2.1 Density and geometry requirements

In order to constrain the distance-redshift relation at $z > 0.6$ using the BAO, we need a galaxy sample that covers the volume of the universe observable at this redshift. In this section we derive the required mean number density of galaxy, $\bar{n}(z)$, and the area to be covered in order to observe the BAO feature at the one percent level.

¹ <http://sumire.ipmu.jp/en/>

² <http://sci.esa.int/euclid>

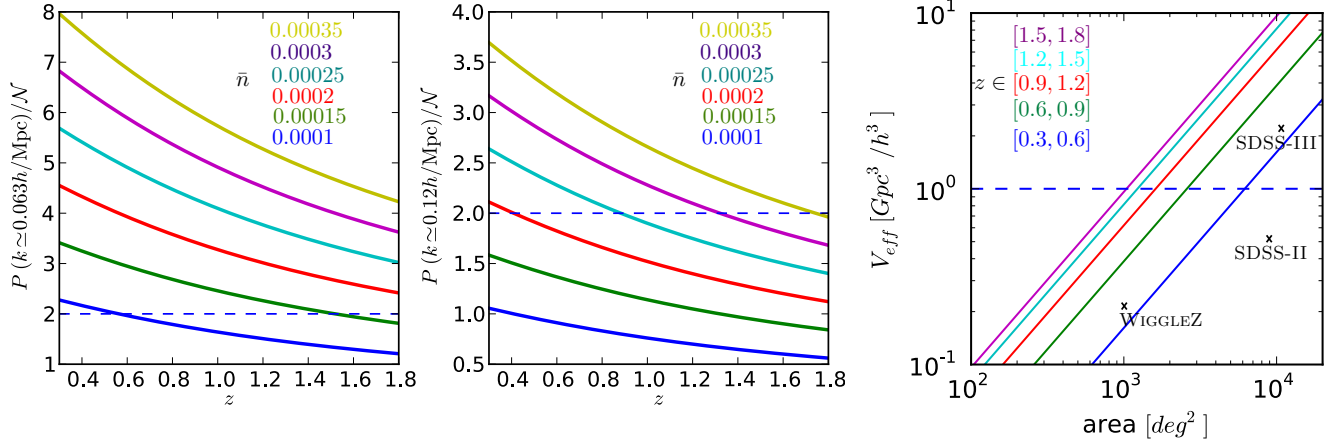


Figure 1. $P/N = \bar{n}P$, ratio of the fiducial power spectrum over the shot noise as a function of redshift at $k \approx 0.063$ (left) and at $k \approx 0.12$ (center) for $\bar{n} \in [1, 3.5] \cdot 10^{-4} h^3 \text{Mpc}^{-3}$. (Right) Effective volume in $\text{Gpc}^3 h^{-3}$ sampled as a function of sky coverage, for five different redshift bins from 0.3 to 1.8, the sampling density used for each bin is given in the column $\bar{n}(k_2)$ of Table 1. To reach a comoving volume of $1 \text{ Gpc}^3 h^{-3}$ over the redshift range $[0.6, 0.9]$, it is necessary to cover about 2500 deg^2 .

The statistical errors in the measure of the power spectrum of galaxies $P(k, z)$, evaluated at redshift z and at scale k , arise from sample variance and shot noise (Kaiser 1986). Denoting the latter as $N(z) = 1/\bar{n}(z)$, to measure a significant signal the minimal requirement is

$$\bar{n}(z)P(k, z) = \frac{P(k, z)}{N(z)} \gtrsim 2. \quad (1)$$

As the amplitude of the power spectrum decreases with redshift, the required density increases with redshift. *e.g.*, at $z = 0.6$, we need a galaxy density of $\bar{n} = 2.1 \times 10^{-4} h^3 \text{Mpc}^{-3}$; at $z = 1.5$, $\bar{n} = 3.2 \times 10^{-4} h^3 \text{Mpc}^{-3}$. The full trend in redshift bins is given in Table 1 and in Figures 1 a) and b) which show equation (1) as a function of redshift for $k \approx 0.063 h \text{Mpc}^{-1}$ and $k \approx 0.12 h \text{Mpc}^{-1}$ (the location of the first and the second harmonics of the BAO peak in the linear power spectrum).

In order to minimize the sample variance, we must sample the largest possible volume (a volume of $1 \text{ Gpc}^3 h^{-3}$ roughly corresponds to a precision in the BAO scale measurement of 5 percent). To quantify this calculation, we use the effective volume sampled V_{eff} , defined as (Tegmark 1997b)

$$V_{\text{eff}}(k) = 4\pi \int dr r^2 \left[\frac{\bar{n}(r)b^2(z)P(r, k)}{1 + \bar{n}(r)b^2(z)P(r, k)} \right]^2. \quad (2)$$

In this calculation, we assume a linear bias according to the DEEP2 study by Coil et al. (2008) that varies according to the redshift as $b(z) = b_0(1 + z)$, with $b(z = 0.8) = 1.3$. The bias could be larger for the more luminous ELGs, that are thought to be the progenitors of massive red galaxies (Cooper et al. 2008). We shall evaluate the bias of ELGs more precisely in a future paper. The corresponding area to be surveyed in order to reach $V_{\text{eff}} \sim 1 \text{ Gpc}^3 h^{-3}$ is shown in Table 1, setting redshift bins of width $\Delta z = 0.3$ from $z = 0.3$ to $z = 1.8$. The Figure 1 c) shows the behavior of V_{eff} as a function of the area for a given slice of redshift with \bar{n} given in the third column of Table 1. For the redshift range $[0.6, 0.9]$ the survey area must be $\gtrsim 2,500 \text{ deg}^2$. For the redshift range $[0.9, 1.2]$ the survey area must be $\gtrsim 1,600 \text{ deg}^2$. The observation of $[0.6, 1.7]$ with a single galaxy selection thus needs $2,500 \text{ deg}^2$ to sample the BAO at all redshifts.

Reconstruction of the galaxy field

To obtain a high precision on the measure of the BAO scale, it is necessary to correct the 2-point correlation function from the dominant non-linear effect of clustering. The bulk flows at a scale of $20 h^{-1} \text{Mpc}$ that form large scale structures smear the BAO peak: it is smoothed by the velocity of pairs (At redshift 1 the rms displacement for biased tracers due to bulk flows is $8.5 h^{-1} \text{Mpc}$ in real space and $17 h^{-1} \text{Mpc}$ in redshift space) (Eisenstein et al. 2007a,b).

Reconstruction consists in correcting this smoothing effect. The key quantity that allows reconstruction on a data sample is the smoothing scale used to reconstruct the velocity field and should be as close to $5 h^{-1} \text{Mpc}$ as possible in order to measure the bulk flows without being biased by other non-linear effects that occur on smaller scales.

The reconstruction algorithm applied on the SDSS-II Data Release 7 (Abazajian et al. 2009) LRG sample sharpens the BAO feature and reduces the errors from 3.5 percent to 1.9 percent. This sample has a density of tracers of $10^{-4} h^3 \text{Mpc}^{-3}$ and the optimum smoothing applied is $15 h^{-1} \text{Mpc}$ (Padmanabhan et al. 2012). On the SDSS-III/BOSS data in our study (different patches cover $3,275 \text{ deg}^2$ on a total of $10,000 \text{ deg}^2$), reconstruction sharpens the BAO peak allowing a detection at high significance, but does not significantly improve the precision on the distance measure due to the gaps in the current survey (see Anderson et al. 2012).

To allow an optimum reconstruction using a smoothing three times smaller ($5 h^{-1} \text{Mpc}$) it is necessary to have a dense and contiguous galaxy survey : gaps in the survey footprint smaller than 1 Mpc and a sampling density higher than $3 \times 10^{-4} h^3 \text{Mpc}^{-3}$. This setting should reduce the sample variance error on the acoustic scale by a factor four.

2.2 Observational requirements

A mean galaxy density of $3 \times 10^{-4} h^3 \text{Mpc}^{-3}$ can be reached by a projected density of 162 galaxies deg^{-2} with $0.6 < z < 0.9$, 261 deg^{-2} with $0.9 < z < 1.2$, 354 with $1.2 < z < 1.5$, and 589 with $1.5 < z < 1.8$. Considering a simple case where a survey is divided

in three depths, the shallow one covering $2,500 \text{ deg}^2$ should contain 419,000 galaxies; the medium 421,000 galaxies over $1,600 \text{ deg}^2$; and the deep 435,000 galaxies over $1,200 \text{ deg}^2$. This represents a survey containing 1,350,000 measured redshifts in the redshift range $[0.6, 1.5]$. The challenge is to build a selection function that enhances the observation of these projected densities.

Given a ground-based large spectroscopic program that measures 1.5×10^6 spectra (it corresponds to about 4 years of dark time operations on SDSS telescope dedicated to ELGs), the challenge is to define a selection criterion that samples galaxies to measure the BAO on the greatest redshift range possible. We define the selection efficiency as the ratio of the number of spectra in the desired redshift range and the number of measured spectra. The example in the previous paragraph needs a selection with an efficiency of $1.35/1.5 \sim 90$ percent.

2.3 Previous galaxy targets selections

To reach densities of tracers $\geq 10^{-4} h^3 \text{ Mpc}^{-3}$ at $z > 0.6$ with a high efficiency, a simple magnitude cut is not enough. Such a selection would be largely dominated by low-redshift galaxies. The use of colour selections is necessary to narrow the redshift range of the target selection for observations.

SDSS-I/II galaxies are selected with visible colours in the red end of the colour distribution of galaxies, resulting in a sample of LRG and not ELGs (Eisenstein et al. 2001). The projected density of LRG is $\sim 120 \text{ deg}^{-2}$ with a peak in the redshift distribution at $z \sim 0.35$. With the SDSS-I/II LRG sample, the distance redshift relation was reconstructed at 2 percent at $z = 0.35$.

BOSS has currently completed about half of its observation plan. The tracers used by BOSS are, as SDSS-I/II LRG, selected in the red end of the color distribution of galaxies, they are called CMASS (it stands for ‘constant mass’ galaxies) and the selection will be detailed in Padmanabhan et al. in prep. (2012). The current BAO detection using the data release 9 (a third of the observation plan) with the CMASS tracers at $z \sim 0.57$ has a 6.7σ significance (Anderson et al. 2012).

WiggleZ blue galaxies are selected using UV and visible colours: they have a density of 240 galaxies deg^{-2} and a peak in the redshift distribution around $z = 0.6$ (Drinkwater et al. 2010). The WiggleZ experiment has obtained a 4.9σ detection of the BAO peak at $z = 0.6$ (Blake et al. 2011).

At their peak density, both of these BAO surveys reach a galaxy density of $3 \times 10^{-4} h^3 \text{ Mpc}^{-3}$, which guarantees a significant detection of the BAO.

Galaxy selections beyond $z = 0.6$ were already performed by surveys such as the VIMOS-VLT Deep Survey³ (VVDS, see Le Fèvre et al. 2005a), DEEP2⁴ (see Davis et al. 2003) or Vimos Public Extragalactic Redshift Survey⁵ (VIPERS, see Guzzo et al. 2012, in preparation), but they are not tuned for a BAO analysis. The DEEP2 Survey selected galaxies using BRI photometry in the redshift range $0.75-1.4$ on a few square degrees with a redshift success of 75 percent using the Keck Observatory. It studied the evolution of properties of galaxies and the evolution of the clustering of galaxies compared to samples at low-redshift. In particular, insights in galaxy clustering to $z = 1$ brings a strong knowledge about the bias of these galaxies (Coil et al. 2008). The VVDS wide survey

observed 20 000 redshift on 4 deg^2 limited to $I_{AB} < 22.5$ (Garilli et al. 2008); they studied the properties of the galaxy population to redshift 1.2 and the small scale clustering around $z = 1$. The VIPERS survey maps the large scale distribution of 100 000 galaxies on 24 deg^2 in the redshift range $0.5 - 1.2$ to study mainly clustering and redshift space distortions. Their colour selection, based on *ugri* bands, is described in more detail in the section 6.

3 COLOR SELECTIONS

Our aim is to explore different colour selections that focus on galaxies located in $0.6 < z < 1.7$ with strong emission lines, so that assigning redshifts to these galaxies is feasible within short exposure times (typically one hour of integration on the 2.5m SDSS telescope). The methodology used here has been first explored and experimented by Davis et al. (2003), Adelberger et al. 2004, Drinkwater et al. 2010. Adelberger et al. (2004) derived different colour selections for faint galaxies (with $23 < R < 25.5$) at redshifts $1 < z < 3$ based on the Great Observatories Origins Deep Survey data (GOODS, see Dickinson et al. 2003). Drinkwater et al. (2010) selected ELGs using UV photometry from the Medium Imaging Survey of the GALaxy EVolution EXplorer (MIS-GALEX, see Martin et al. 2005) data combined with SDSS, to obtain a final density of 238 ELGs per square degree with $0.2 < z < 0.8$ over ~ 800 square degrees.

Our motivation is to probe much wider surveys than GOODS or GALEX (ultimately a few thousands square degrees) and to concentrate on intrinsically more luminous galaxies (typically with $g < 23.5$) with a redshift distribution extended to redshift 1.7.

The selection criteria studied in this work are designed for a ground-based survey and more specifically for the SDSS telescope, a 2.5m telescope located at Apache Point Observatory (New Mexico, USA), which has a *unique* wide field of view to carry out LSS studies (Gunn et al. 2006). The current BOSS spectrographs cover a wavelength range of $3600 - 10200 \text{ \AA}$. Its spectral resolution, defined by the wavelength divided by the resolution element, varies from $R \sim 1,600$ at $3,600 \text{ \AA}$ to $R \sim 3,000$ at $10,000 \text{ \AA}$ (Eisenstein et al. 2011). The highest redshift detectable with the [OII] emission line doublet ($\lambda 3727, \lambda 3729$) is thus $z_{\text{max}} = 1.7$.

To select ELGs in the redshift range $[0.6, 1.7]$ we have explored two different selection schemes: first using *u, g, r* photometry and secondly using *g, r, i* photometry.

3.1 Photometric data properties: SDSS, CFHT-LS and COSMOS

The photometric SDSS survey, delivered under the data release 8 (DR8, Aihara et al. 2011), covers 14,555 square degrees in the 5 photometric bands *u, g, r, i, z*. It is the largest volume multi-color extragalactic photometric survey available today. The 3σ magnitude depths are: $u = 22.0$, $g = 22.2$, $r = 22.2$, $i = 21.3$; see Fukugita et al. (1996) for the description of the filters and Gunn et al. (1998) for the characteristics of the camera. The magnitudes we use are corrected from galactic extinction.

The Canada France Hawaii Telescope Legacy Survey⁶ (hereafter CFHTLS) covers $\sim 155 \text{ deg}^2$ in the *u, g, r, i, z* bands. The transmission curves of the filters differ slightly⁷ from SDSS. The data

³ <http://cesam.oamp.fr/vvdsproject/>

⁴ <http://deep.berkeley.edu/index.html>

⁵ <http://vipers.inaf.it/project.html>

⁶ <http://www.cfht.hawaii.edu/Science/CFHLS/>

⁷ <http://cadwww.dao.nrc.ca/megapipe/docs/filters.html>

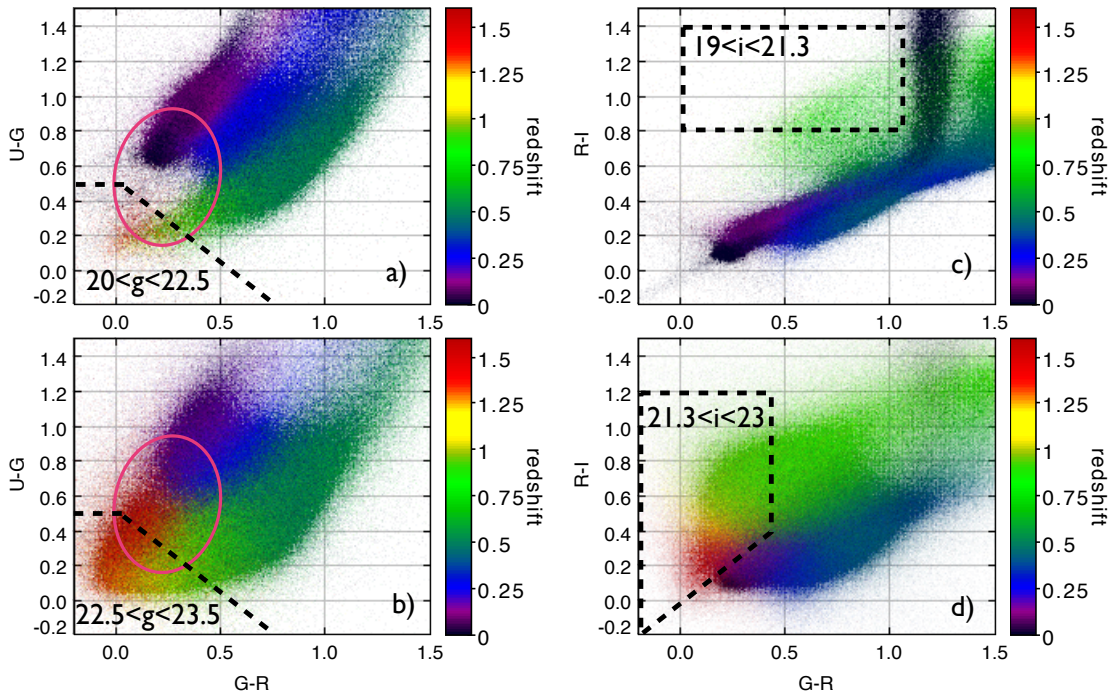


Figure 3. Color-color diagrams tinted according to CFHT-LS photometric redshift. Colour selections are indicated with the dashed boxes. Quasars, when overlapping with the colour selection, are located in the pink ellipse. The stellar sequence appears in black. **a)** The bright *ugr* colour selection: $u-g$ vs $g-r$ for $20 < g < 22.5$. In this area the overall density of targets is low. **b)** The faint *ugr* colour selection where the magnitude range is $22.5 < g < 23.5$. The density of available targets increases and the stellar sequence is diminished. **c)** The bright *gri* colour selection: $r-i$ vs $g-r$ diagram for $19 < i < 21.3$. The high-redshift targets are not as visible as in the *ugr* plot. The target density is also small. **d)** The faint *gri* colour selection where the magnitude range is $21.3 < i < 23$. The target density increases and higher redshift targets appear in the blue end of the colour plot while the stellar locus fades. Using SDSS photometry one would obtain similar plots to **a)** and **c)** in terms of target density.

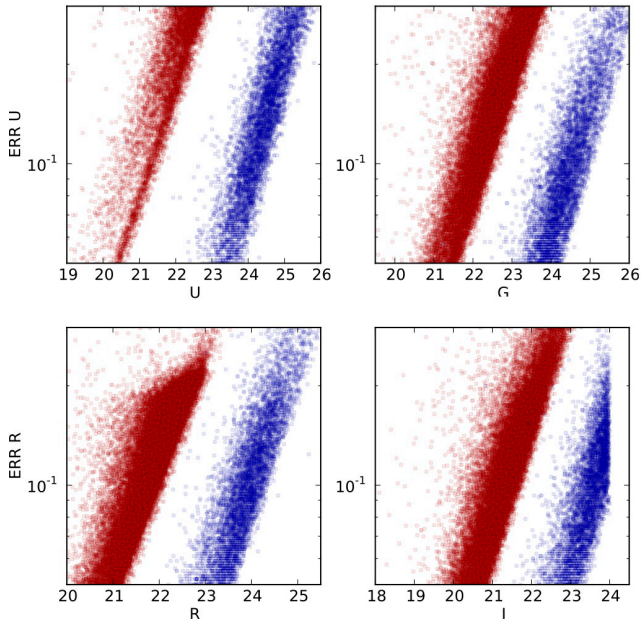


Figure 2. The four bands *ugri* and their precision are illustrated; in red for SDSS photometry; in blue for CFHTLS photometry. The *u* band quality is limiting the precision of the colour selection on SDSS photometry. Note that the photometric redshift CFHTLS catalog is cut at $i = 24$, and the SDSS data is R-selected with $err_R \leq 0.2$.

and cataloging methods are described in the T0006 release document⁸. The 3σ magnitude depths are: $u = 25.3$, $g = 25.5$, $r = 24.8$, $i = 24.5$. The CFHT-LS photometry is ten times (in r and i) to thirty times (in u) deeper than SDSS DR8, however the CFHTLS covers a much smaller field of view than SDSS DR8. The magnitudes we use are corrected from galactic extinction. The CFHT-LS photometric redshift catalogs are presented in Ilbert et al. (2006), and Coupon et al. (2009); the photometric redshift accuracy is estimated to be $\sigma_z < 0.04(1+z)$ for $g \leq 22.5$. This photometric redshift catalog is cut at $i = 24$, beyond which photometric redshifts are highly unreliable. Fig. 2 displays the relative depth between SDSS and CFHT-LS wide surveys in the *u, g, r, i*-bands.

COSMOS is a deep 2 deg^2 survey that has been observed at more than 30 different wavelengths (Scoville et al. 2007). The COSMOS photometric catalog is described in Capak et al. (2007) and the photometric redshifts in Ilbert et al. (2009). The COSMOS Mock Catalog, (hereafter CMC; see⁹) is a simulated spectro-photometric catalog based on the COSMOS photometric catalog and its photometric redshift catalog. The magnitudes of an object in any filter can be computed using the photometric redshift best-fit spectral templates (Jouvel et al. 2009, Zoubian et al. 2012, in preparation).

The limiting magnitudes of the CMC in the each band are the same as in the real COSMOS catalog (detection at 5σ in a $3''$ diameter aperture): $u < 26.4$, $g < 27$, $r < 26.8$, $i < 26.2$. For magnitudes

⁸ <http://terapix.iap.fr/cpl/T0006-doc.pdf>

⁹ <http://lamwww.oamp.fr/cosmowiki/RealisticSpectroPhotCat>

in the range $14 < m < 26$ in the g, r, i bands from the Subaru telescope and in the u band from CFHTLS, the CMC contains about 280,000 galaxies in 2 deg^2 to COSMOS depth. The mock catalog also contains a simulated spectrum for each galaxy. These simulated spectra are generated with the templates used to fit COSMOS photometric redshifts. Emission lines are empirically added using Kennicutt calibration laws (Kennicutt 1998; Ilbert et al. 2009), and have been calibrated using zCOSMOS (Lilly et al. 2009) as described in Zoubian et al. 2012, in preparation. The strength of [OII] emission lines was confirmed using DEEP2 and VVDS DEEP luminosity functions (Le Fèvre et al. 2005b; Zhu et al. 2009). Finally a host galaxy extinction law is applied to each spectrum. Predicted observed magnitudes take into account the presence of emission lines.

3.2 Color selections

Based on the COSMOS and CFHT-LS photometric redshifts, we explore two simple colour selection functions using the ugr and gri bands. Fig. 3 shows the targets available in the ugr and gri colour planes. We construct a bright and a faint sample based on the photometric depths of SDSS and CFHT-LS.

3.2.1 ugr selection

The ugr colour selection is defined by $-1 < u-r < 0.5$ and $-1 < g-r < 1$ that selects galaxies at $z \geq 0.6$ and ensures that these galaxies are strongly star-forming ($u-r$ cut). The cut $-1 < u-g < 0.5$ removes all low-redshift galaxies ($z < 0.3$). Finally the magnitude range is $20 < g < 22.5$ and $g < 23.5$ for the bright and the faint samples, resp. Fig. 3 a) and b).

3.2.2 gri selection

The bright gri colour selection is defined by the range $19 < i < 21.3$. We select blue galaxies at $z \sim 0.8$ with $0.8 < r-i < 1.4$ and $-0.2 < g-r < 1.1$ (Fig. 3 c). In the faint range $21.3 < i < 23$, we tilt the selection to select higher redshifts with $-0.4 < g-r < 0.4$, $-0.2 < r-i < 1.2$ and $g-r < r-i$ (Fig. 3 d).

3.3 Predicted properties of the selected samples

The ugr colour selection avoids the stellar sequence, but not the quasar sequence. Hence, the contamination of the ugr selection by point-source objects is primarily due to quasars; see Fig. 3 a) and b). The resulting photometric-redshift distribution as derived from the CFHT-LS photometric redshift catalog has a wide span in redshift, covering $0.6 < z < 2$ as shown in Fig. 4. The distribution is centered at $z = 1.3$ for the bright and the faint sample with a scatter of 0.3 (see Table 2). The expected [OII] fluxes are computed from the CMC catalog and are shown in Fig. 4. For 90 percent of galaxies in the faint sample, the predicted flux is above $10.6 \times 10^{-17} \text{ erg cm}^{-2} \text{ s}^{-1}$. The bright sample galaxies show strong emission lines.

The gri selection avoids both the stellar sequence and the quasar sequence; see Fig. 3 c) and d). Thus the contamination from point-sources should be minimal. Fig. 4 shows the photometric redshift distribution of the gri selection applied to CFHT photometry. The redshifts are centered at $z = 0.8$ for the bright and 1.0 for the faint sample (see Table 2). The expected [OII] flux, computed with

the CMC catalog, is shown in Fig. 4. Emissions are weaker than for the ugr selection as expected.

The different selections shown in Fig. 3 and Fig 4 are summarized in Table 2, which contains the number densities available, mean magnitudes, mean redshifts, and mean [OII] fluxes (when available) of the different samples considered. We have lower densities in the CMC than in the CFHT-LS catalog. This is probably due to cosmic variance as the CMC only covers 2 deg^2 .

The SDSS colour-selected samples are complete for the bright samples at $g < 22.5$ and $i < 21.3$, not for the faint samples. The CFHTLS-selected samples are complete for both the bright and faint samples; see Fig. 5, where the total cumulative number counts (solid line) of the ugr and gri colour-selected samples are plotted as a function of g and i bands respectively. On the bright end of this Figure, although both photometry are complete at the bright limit, we note a discrepancy between the total amount of target selected on CFHT and SDSS that implies selections on CFHT are denser than on SDSS (difference between the red and blue solid lines). This is due to the transposition of the color selection from one photometric system to the other. In fact, we select targets on SDSS with a transposed criterion from CFHT using the calibrations by Regnault et al. (2009). The transposed criterion is as tight as the original. But as the errors on the magnitude are larger in the SDSS system, their colour distributions are more spread. Therefore the SDSS selection is a little less dense than the CFHT selection.

Targeting the bright range is limited by galaxy density, in the best case one can reach $300 \text{ targets deg}^{-2}$ and it contains point-sources (stars and quasars) and low-redshift galaxies. In the faint range, the target density is ten times greater, but the exposure time necessary to assign a reliable redshift will be much longer (one magnitude deeper for a continuum-based redshift roughly corresponds to an exposure five times longer). The stellar, quasars and low-redshift contamination is smaller in the faint range. Fig. 4 shows the distributions in redshift and in [OII] flux we expect given a magnitude range and a colour criterion within the framework of the CMC simulation. The main trend is that the ugr selection identifies strong [OII] emitters out to $z \sim 2$ where the gri peaks at redshift 1 and extends to 1.4 with weaker [OII] emitters.

We also used a criterion to split targets in terms of compact and extended sources, which is illustrated in Fig. 5. For CFHT-LS we have used the half-light radius (r_2 value, to be compared to the r_2^{limit} value which defines the maximal size of the PSF at the location of the object considered - see Coupon et al 2009 and CFHT-LS T0006 release document) to divide the sample into compact and extended objects. For SDSS we used the “TYPE” flag, which separates compact (TYPE=6) from extended objects (TYPE=3). For the ugr colour selection, the number counts are dominated by compact blue objects (quasars) at $g \leq 22.2$. At $g \geq 22.2$ the counts are dominated by extended ELGs. For comparison we show in Fig. 5 the cumulative counts of the XDQSO catalog from Bovy et al. (2011) who identified quasars in the SDSS limited to $g < 21.5$. We notice an excellent match with the bright (compact) ugr colour-selected objects. For the gri colour selection, there is a low contamination by compact objects because the colour box does not overlap with either the stellar or the quasar sequence.

4 ELG OBSERVATIONS

To test the reliability of both the bright ugr ($g < 22.5$) and the bright gri ($i < 21.3$) colour selections, we have conducted a set of dedicated observations, as part of the “Emission Line Galaxy

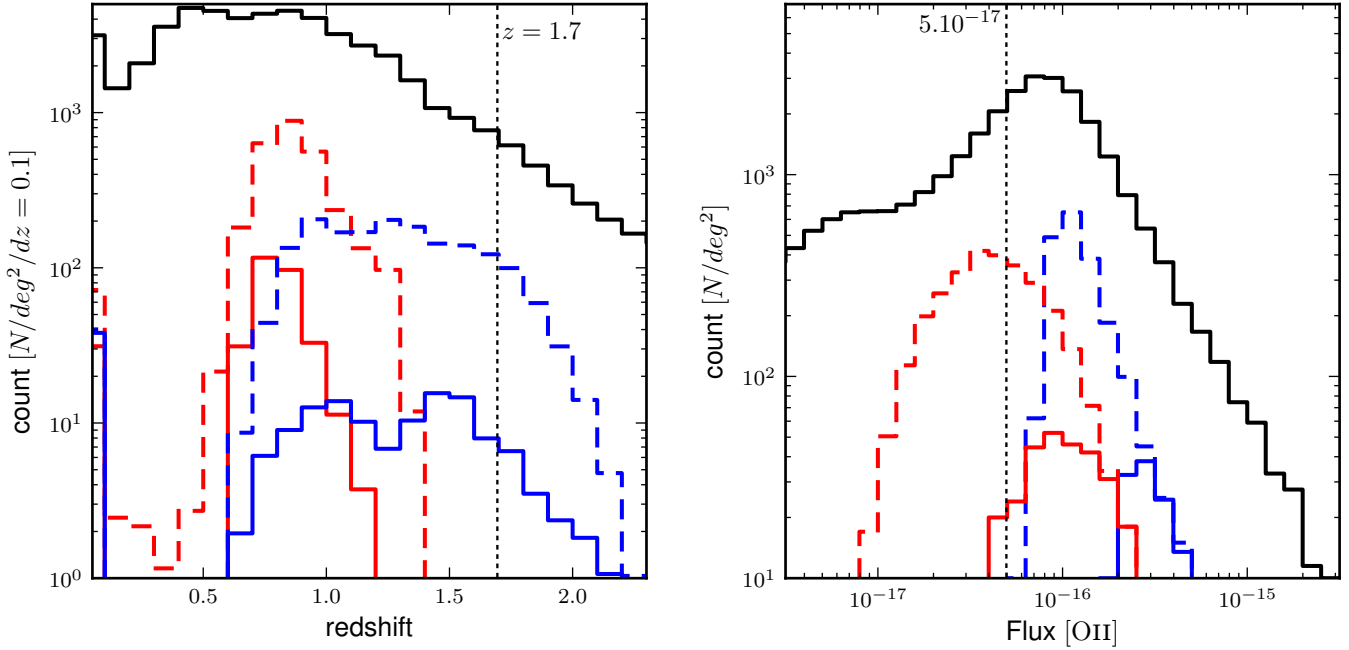


Figure 4. Redshift and line flux distribution for various color selections. The blue solid line is the *u_{gr}* selection limited to $20 < g < 22.5$. The blue dashed line is the *u_{gr}* selection limited to $22.5 < g < 23.5$. The red solid line is the *g_{ri}* selection limited to $19 < i < 21.3$. The red dashed line is the *g_{ri}* selection limited to $21.3 < i < 23.0$. **Left.** Photometric redshift distribution from the CFHT-LS catalog. Black solid line: no colour selection, but limited to $i < 24$. The *u_{gr}* selection is more spread in redshift than the *g_{ri}* selection. The vertical dashed line indicates the upper limit of $z = 1.7$ that corresponds to [OII] emission lines at $\sim 1\mu\text{m}$. **Right.** Expected [OII] flux distribution from the CMC simulation. The black solid line is the complete CMC catalog. The *u_{gr}* selection identifies stronger line emitters than the *g_{ri}* selection scheme. The vertical dashed line indicates the expected mean sensitivity of BOSS in 1h exposure, $5 \times 10^{-17} \text{ erg s}^{-1} \text{ cm}^{-2}$.

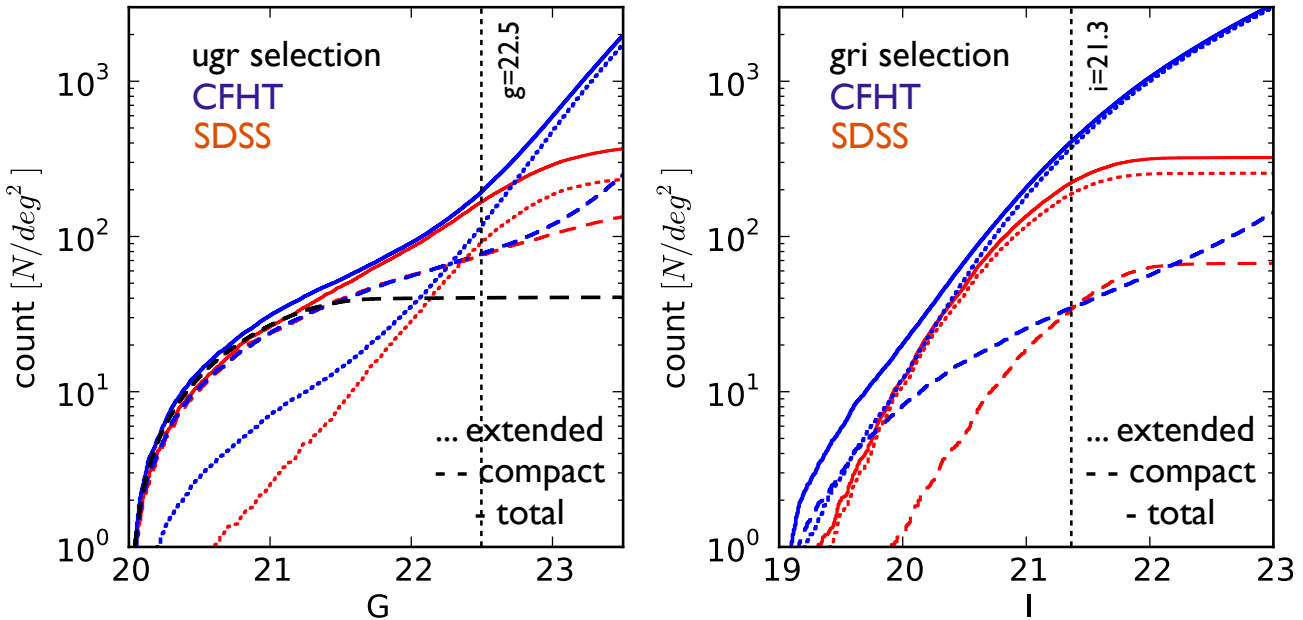


Figure 5. Cumulative number counts per square degree of both colour selections using SDSS photometry (in red) and CFHTLS photometry (in blue). The solid line is the whole selection, while the dashed line is for compact (star-like) objects and the dotted line represents extended objects. On the left is the *u_{gr}* selection and on the right is the *g_{ri}* selection. The black dashed line represents objects from the XDQSO catalog that have a probability of being a quasar that is greater than 90 percent (Bovy et al. 2011) (the quasar identifications are limited to $g = 21.5$).

Table 2. Properties of the colour-selected samples. ‘b’ stands for bright ($20 < g < 22.5$ for *ugr* or $19 < i < 21.3$ for *gri*) and ‘f’ for faint ($22.5 < g < 23.5$ for *ugr* or $21.3 < i < 23$ for *gri*). We indicate the mean and standard deviation of the redshift distribution for each set. For the CMC sample, [OII] fluxes are expressed in units of $10^{-17} \text{ erg cm}^{-2} \text{ s}^{-1}$; the median, the first and third quartiles of the flux distribution are indicated. The *ugr* tends to select the highest [OII] fluxes.

selection		#deg ⁻²	\bar{u}	\bar{g}	\bar{r}	\bar{i}	\bar{z}	σ_z	$f_{\text{[OII]}}$	$Q^1_{f_{\text{[OII]}}}$	$Q^3_{f_{\text{[OII]}}}$	
CMC	<i>ugr</i>	b	130.0	21.98	21.87	21.69	-	1.25	0.53	61.74	46.47	88.39
		f	1450.8	23.27	23.18	22.98	-	1.19	0.38	16.60	13.06	22.26
	<i>gri</i>	b	257.2	-	22.69	21.87	20.93	0.80	0.21	13.85	8.65	22.21
		f	2170.5	-	23.34	23.09	22.55	0.93	0.31	10.23	6.83	15.99
CFHT-W1	<i>ugr</i>	b	193.3	21.95	21.8	21.7	-	1.28	0.38			
		f	1766.8	23.37	23.19	23.07	-	1.29	0.31			
	<i>gri</i>	b	361.4	-	22.62	21.8	20.82	0.81	0.11			
		f	3317.5	-	23.34	23.11	22.55	1.03	0.35			
CFHT-W3	<i>ugr</i>	b	232.2	21.89	21.76	21.69	-	1.27	0.37			
		f	1679.1	23.36	23.18	23.06	-	1.28	0.31			
	<i>gri</i>	b	391.6	-	22.62	21.78	20.8	0.82	0.1			
		f	3334.2	-	23.34	23.11	22.54	1.03	0.33			
SDSS	<i>ugr</i>	b	166.96	21.76	21.77	21.52	-					
	<i>gri</i>	b	204.96	-	22.57	21.75	20.76					

SDSS-III/BOSS ancillary program”. The observations were conducted between Autumn 2010 and Spring 2011 using the SDSS telescope with the BOSS spectrograph at Apache Point Observatory. A total of $\sim 2,000$ spectra, observed 4 times 15 minutes, were taken in different fields: namely, in the Stripe 82 (using single epoch SDSS photometry for colour selection) and in the CFHT-LS W1, W3 and W4 wide fields (using CFHT-LS photometry). This data set was released in the SDSS-III Data Release 9¹⁰.

4.1 Description of SDSS-III/BOSS spectra

We used the SDSS photometric catalog (Aihara et al. 2011) to select 313 objects according to their *ugr* colours located in the Stripe-82 and 899 objects selected according to their *gri* colours in the CFHT-LS W3 field. In addition we used the CFHT-LS photometry to select 878 *ugr* targets in the CFHT-LS W1 field, and 391 *gri* targets in the CFHT-LS W3 field for observation. The spectra are available in SDSS Data Release 9 and flagged ‘ELG’.

All of these spectra were manually inspected to confirm or correct the redshifts produced by two different pipelines (zCODE and its modified version that we used to fit the [OII] emission line doublet). As the BOSS pipeline redshift measurement is designed to fit LRG continuum some ELG with no continuum were assigned wrong redshifts. To classify the observed objects, we have defined seven sub-categories :

Objects with secure redshifts

- ‘ELG’, Emission-line galaxy (redshift determined with multiple emission lines). Usually these spectra have a weak ‘blue’ continuum and lack a ‘red’ continuum. Empirically, using PLATEFIT VIMOS pipeline output, this class corresponds to a spectrum with more than two emission lines with observed equivalent widths $EW \leq -6\text{\AA}$; see examples in Appendix A.

- ‘RG’, Red Galaxy with continuum in the red part of its spectrum, allowing a secure redshift measurement through multiple absorption lines (e.g. Ca K&H, Balmer lines) and the 4000Å break. Some of these objects have also weak emission (E+A galaxies). Empirically their spectra have a mean $D_n(4000)$ of 1.3; where $D_n(4000)$ is the ratio of the continuum level after the break and before the break. These galaxies typically have $i \sim 20$, which is fainter than the CMASS targeted by BOSS.

- ‘QSO’, Quasars, which are identified through multiple broad lines. Examples are given in Fig. A4.

- Stars.

Objects with unreliable redshifts

- ‘Single emission line’: the spectra contain only a single emission line which cannot allow a unique redshift determination. For this population, the CFHT T0006 photometric redshifts are compared to the [OII] redshift (assuming the single emission line is [OII]) in Fig. 6. The two estimates agree very well: 77.7 percent have $(z_{\text{spec}} - z_{\text{phot}})/(1 + z_{\text{spec}}) < 0.1$ for the *gri* selection and 62.7 percent for the *ugr* selection. These galaxies with uncertain redshift tend to have slightly fainter magnitudes with a mean CFHT *g* magnitude at 22.6 and a scatter of 0.6, whereas for the whole ELGs is 22.4 with a scatter of 0.4.

- ‘Low continuum’ spectra that show a 4000Å break too weak for a secure redshift estimate. The agreement between photometric and spectroscopic redshift estimation is excellent: 84.6 percent within 10 percent errors; see Fig. 6.

- ‘Bad data’, the spectrum is either featureless, extremely noisy or both.

The detailed physical properties of the ELGs are discussed in section 5 and a number of representative spectra are displayed in Appendix A.

4.2 Redshift Identification

The results of the observations are summarized by categories in Table 3.

¹⁰ <http://dr9.sdss3.org/>

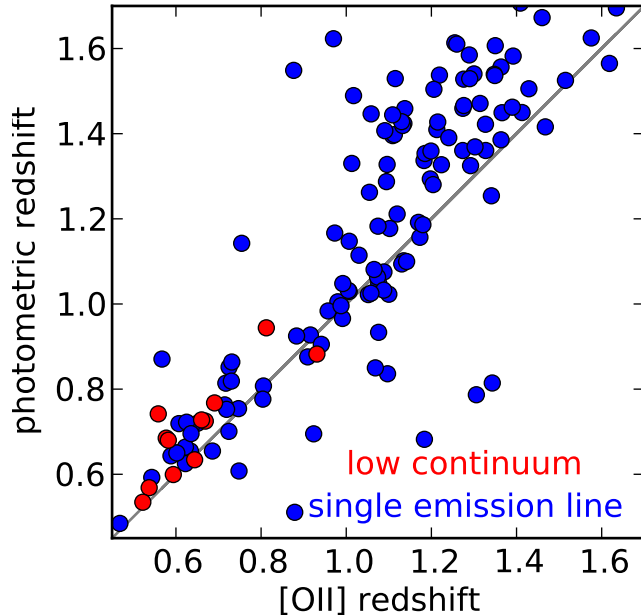


Figure 6. T0006 CFHT-LS photometric redshifts of single emission line and low continuum galaxies observed against [OII] redshift. A strong correlation is clearly evident. A slight systematic over-estimation of the photometric redshift is visible above redshift 1.2 (these photometric redshifts were calibrated below 1.2).

For the targets selected using SDSS photometry and with the *ugr* selection : 32 percent are ELGs at a redshift $z > 0.6$ (100 spectra). The low-redshift ELGs represent 32 percent of the observed targets (101 spectra). The other categories are : 65 ‘bad data’ (20 percent), 30 quasars (10 percent), 10 stars (3.5 percent), and 7 red galaxies with $z < 0.6$ (2.5 percent). With the *gri*-selection, 57 percent of the targets are at $z > 0.6$. However, still 21 percent of the spectra fall into the bad data class.

Using CFHTLS photometry 46 percent of targets are ELGs at $z > 0.6$ and 14 percent are quasars with the *ugr* selection. With the *gri*-selection, 73 percent are galaxies at $z > 0.6$, five-sixths of which are ELG.

For both selections, targeting with CFHTLS is more efficient than with SDSS. The complete classification of observed targets is in Table 3. The redshift distribution of the observed objects is compared to the distributions from the BOSS and WiggleZ current BAO experiments in Fig. 7. The Figure shows that *ugr* and *gri* target selections enable a BAO study at higher redshifts. With a joint selection, we can reach the requirements described in Table 1 to detect BAO feature to redshift 1.

4.3 Comparison of measured ELGs with the CMC forecasts

To investigate the expected purity of ELG galaxies samples, we created mock catalogs covering redshifts between 0.6 and 1.7. Continuum spectra of ELGs were generated from the Cosmos Mock Catalog and emission lines were added according to the modeling described in Jouvel et al. (2009). Two simulated galaxy catalogs were built, one for each colour selection function (*ugr* and *gri*). Each synthetic spectrum was affected by sky and photon noise as if observed by BOSS spectrographs, by using the SPECSIM1D software.

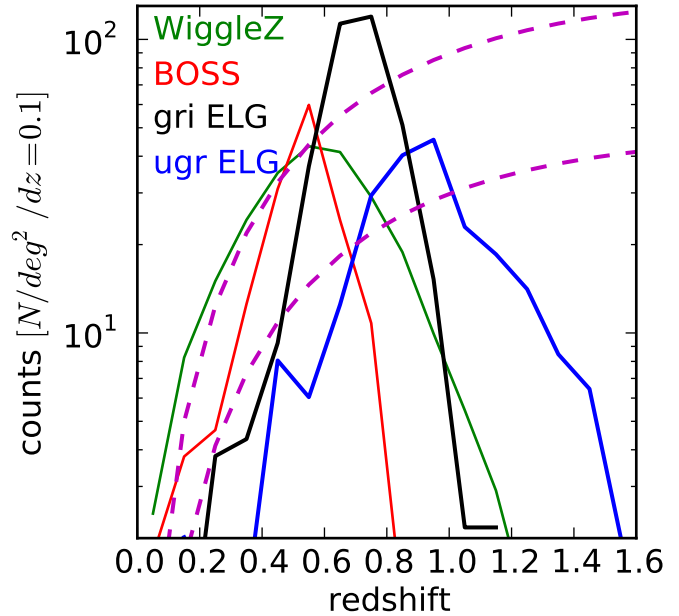


Figure 7. Observed redshift distribution for the *ugr* ELGs (blue), the *gri* ELGs (black) compared to the distribution of galaxies from BOSS (red) and WiggleZ (green). Magenta lines represent constant density of galaxies at 1 and $3 \times 10^{-4} h^3 \text{ Mpc}^{-3}$, it constitutes our density goals.

We simulated a set of four exposures of 900 seconds each. The resulting simulated spectra were then analyzed by the zCODE pipeline (Cannon et al. 2006) to extract the spectroscopic redshift. As our targets are mainly emission line galaxies, we only use the redshift estimate based on fitting discrete emission line templates in Fourier space over all z .

We address the flux measurement of emission lines. This exercise was conducted using the PLATEFIT VIMOS software developed by Lamareille et al. (2009). This software is based on the PLATEFIT software that was developed to analyze SDSS spectra (Tremonti et al. 2004a; Brinchmann et al. 2004). The PLATEFIT VIMOS software was developed to measure the flux of all emission lines after removing the stellar continuum and absorption lines from lower resolution and lower signal-to-noise ratio spectra (Lamareille et al. 2006). The stellar component of each spectrum is fit by a non-negative linear combination of 30 single stellar population templates with different ages (0.005, 0.025, 0.10, 0.29, 0.64, 0.90, 1.4, 2.5, 5 and 11 Gyr) and metallicities (0.2, 1 and $2.5 Z_{\odot}$). These templates have been derived using the Bruzual & Charlot (2003) libraries and have been resampled to the velocity dispersion of VVDS spectra. The dust attenuation in the stellar population model is left as a free parameter. Foreground dust attenuation from the Milky Way has been corrected using the Schlegel et al. (1998) maps.

After removal of the stellar component, the emission lines are fit as a single nebular spectrum made of a sum of Gaussians at specified wavelengths. All emission lines are set to have the same width, with the exception of the [OII] $\lambda 3727$ line which is a doublet of two lines at 3726 and 3729 Å that appear broadened compared to other single lines. Detected emission lines may also be removed from the original spectrum in order to obtain the observed stellar spectrum and measure indices, as well as emission-line equivalent widths. The underlying continuum is obtained by smoothing the

Table 3. Observed objects split in categories.

Type	<i>gri</i> selection				<i>ugr</i> selection			
	<i>SDSS</i> selection		<i>CFHTLS</i> selection		<i>SDSS</i> selection		<i>CFHTLS</i> selection	
	Number	%	Number	%	Number	%	Number	%
ELG($z > 0.6$)	450	50	240	61	100	32	402	46
ELG($z < 0.6$)	60	7	3	1	101	32	84	9
RG($z > 0.6$)	73	8	46	12	0	0	0	0
RG($z < 0.6$)	30	3	0	0	7	3	0	0
single emission line	36	4	12	3	0	0	102	12
low continuum	13	1	1	0	0	0	0	0
QSO	8	1	5	1	30	10	126	14
stars	44	5	12	3	10	3	6	1
bad data	185	21	72	18	65	20	158	18
total	899	100	391	100	313	100	878	100

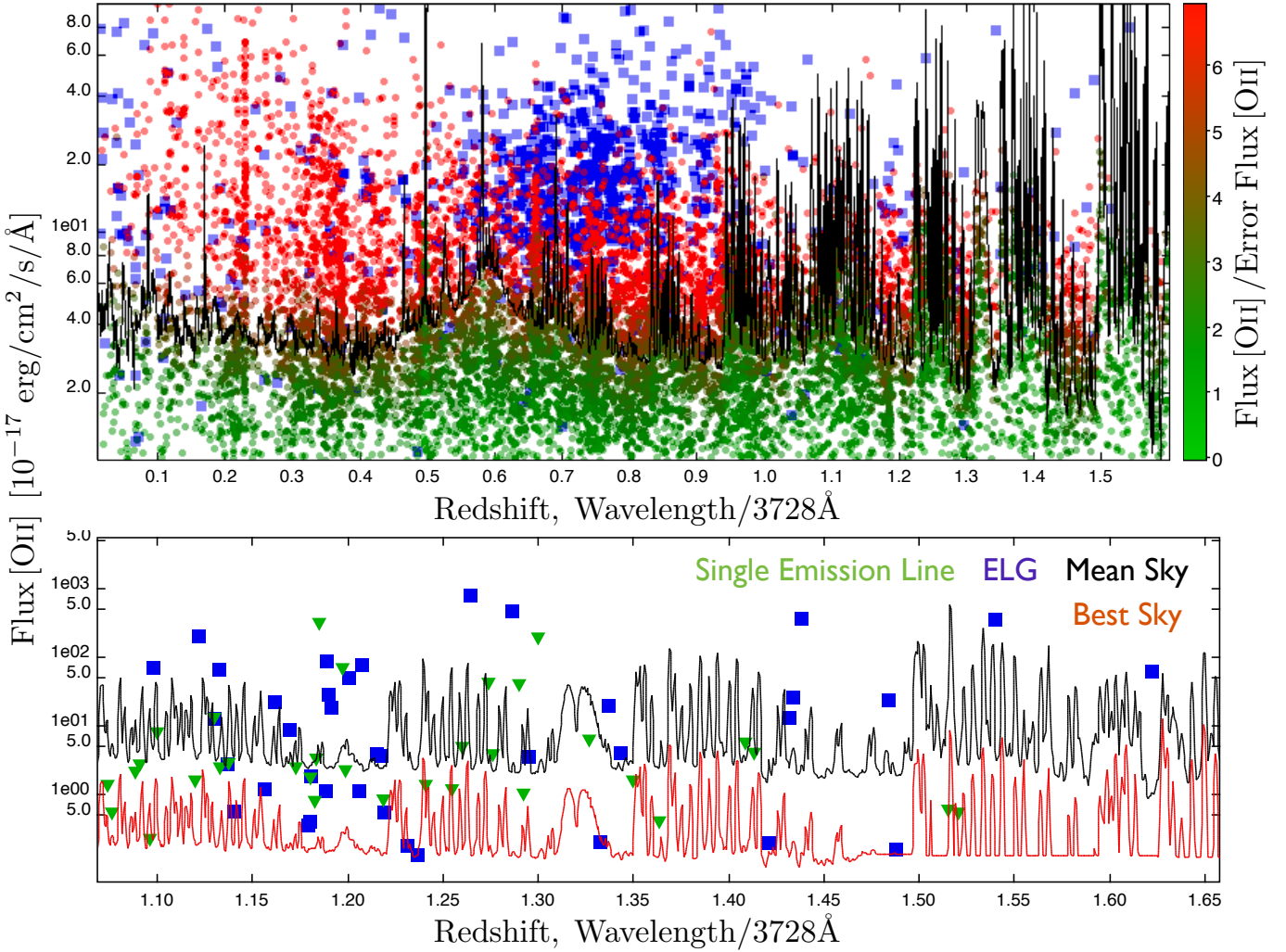


Figure 8. Top : Flux detected in the [OII] doublet (green or red filled circle for a simulated spectrum and blue filled square for a real galaxy observation) versus redshift. The simulation is coloured according to the measured line flux divided by the error. The black solid line represents a typical sky as observed by BOSS spectrograph; the 5σ detections of [OII] follow the sky flux. The [OII] detections above 5σ (red circles) follow the tendency of the sky fluctuations : a 5σ detection in a zone with a high sky requires a larger emitted flux. The data are scaled to match a 1 hour exposure on the 2.5m SDSS telescope. The redshifts below the sky flux are assigned using other emission lines or the information in the continuum. **Bottom:** : An expansion of the top panel using $z > 1$ detections. Only measured galaxies are plotted upon the mean sky (black) and the best sky (red) of APO.

stellar spectrum. Equivalent widths are then measured via direct integration over a 5σ bandpass of the emission-line Gaussian model divided by the underlying continuum. Then emission lines fluxes are measured for each simulated spectra using the extracted redshift from zCODE and the true redshift for cross-checks.

We consider that a redshift has been successfully measured if $\Delta z/(1+z) < 0.001$. We believe that this threshold could be lowered to 10^{-4} in the future by using a more advanced redshift solver. Using the current pipeline, we can distinguish these two regimes.

The first regime is the redshift range $z < 1.0$. Many emission lines ([OII], H β , [OIII]) are present in the SDSS spectrum. For $g < 23.5$, 91 percent of the redshift are measured successfully. Among the remaining 9 percent, catastrophic failures represent 3.5 percent (the pipeline outputs a redshift between 0 and 1.6 with $\Delta z/(1+z) > 0.01$). Inaccurate redshifts represent 3.9 percent (the pipeline outputs a redshift between 0 and 1.6 with $0.001 < \Delta z/(1+z) < 0.01$) and 1.5 percent are not found by the pipeline ($z = -9$ is output).

The second regime is the redshift range $1.0 \leq z < 1.7$: the redshift determination hinges on the identification of the [OII] doublet. For $g < 23.5$, 66.8 percent of the redshifts are measured successfully. 19.1 percent are catastrophic failures and 14.1 percent are inaccurate redshifts. Work is ongoing to improve the redshift measurement efficiency at $z > 1$. In the second regime, the minimum [OII] flux required to compute a reliable redshift depends on the redshift / wavelength, because of the strong OH sky lines in the spectrum. We infer from the observed spectra that to measure a reliable redshift, we require a 5σ detection of the [OII] lines, which means a (blended or not) detection of two peaks in the emission line separated by $2(1+z)$. The detection significance is defined from the 1d spectrum. From the data the faintest 5σ detections are made with a flux of $4 \times 10^{-17} \text{ erg s}^{-1} \text{ cm}^{-2}$ and the brightest 5σ detections need a flux of $2 \times 10^{-16} \text{ erg s}^{-1} \text{ cm}^{-2}$ to be on top of sky lines. The simulation shows the same thresholds; see Fig. 8. The simulation confirms the detection limit we observe. The bottom plot of Fig. 8 raises the issue that the sky time variation has a non-negligible impact on the detection limit of the [OII] emission doublet for redshifts $z > 1.1$. Though this ELG sample is too small to address this issue. In fact the sample was observed during ten different nights and the number of ELG with $z > 1.1$ is less than 60. It is thus not possible to derive a robust trend comparing the [OII] detections to the sky value of each observation. Handling this issue would require a sample of ~ 500 redshifts in $1.1 < z < 1.6$ observed many times over many nights. With such a sample in hands, we could quantify exactly how to optimize the observational strategy.

5 PHYSICAL PROPERTIES OF ELGS

All *ugr* and *gri* ELG spectra were analyzed with two different software packages: the PlateFit VIMOS (Lamareille et al. 2009) and the Portsmouth Spectroscopic Pipeline (Thomas et al. 2012). In this section we discuss the following physical properties of the observed ELGs: redshift, star forming rate (SFR), stellar mass, metallicity and classification of the ELG type (Seyfert 2, LINERs, SFG, composite). Observations a larger samples of ELGs are planned to estimate how these quantities vary over time and with their environment, and also to estimate how the clustering depends on these physical quantities. It is key to replace future BAO tracers in the galaxy formation history. With the current sample, we draw simple trends using means and standard deviation of the observed quantities, and we place the ELGs in the galaxy classification made by Lamareille (2010); Marocco et al. (2011).

5.1 Main Properties

The main properties of the ELGs are shown in the Table 4. The star forming rate was computed using the equation 18 of Argence & Lamareille (2009). The stellar mass was estimated using the CFHTLS *ugriz* photometry. (The errors on the stellar mass using only SDSS photometry were too large to be meaningful, thus the empty cells in the table). The metallicity is estimated using the calibration by Tremonti et al. (2004b). The main trends are :

- The *gri*-selected galaxies of CFHTLS are the more massive galaxies in terms of stellar mass.
- The *ugr* selects stronger star-forming galaxies than *gri* (due to the *u*-band selection). There is a factor of two variations in the strength of the measured oxygen lines.
- The *ugr* selects galaxies that have $12 + \log[OH] \in [8, 9]$ whereas *gri* focuses slightly more on the higher $12 + \log[OH] \approx 9$.
- the SFR appears to be independent of the color selection schemes.

5.2 Classification.

We use a recent classification (Lamareille 2010; Marocco et al. 2011) for the ELG sample. The classification is made using $\log([OIII]/H\beta)$, $\log([OII]/H\beta)$, $D_n(4000)$, and $\log(\max(EW_{[OII]}, EW_{[NeIII]}))$. We compare the ELG sample to zCOSMOS, as zCOSMOS has numerous star forming galaxies in the redshift range we are observing. Fig. 9 a) shows that the zCOSMOS and the *ugr* ELG samples are located in three of the five areas delimited by the classification: Seyfert 2 ('Sy2'), Star Forming Galaxies ('SFG'), and a third region where both mix ('Sy2/SFG'). There are a few LINERs and Composite in either sample. Fig. 9 b) separates the *ugr* galaxies in the 'Sy2/SFG' area into 'SFG' or 'Sy2', and shows that zCOSMOS galaxies from the 'Sy2/SFG' area are both 'Sy2' and 'SFG' where the *ugr* ELGs in the 'Sy2/SFG' area are mostly 'SFG'. The *gri* observed sample is located in the area of Star Forming Galaxies ('SFG'), whether one considers the one selected on CFHT or on SDSS. Finally, the ELG selected, *ugr* or *gri*, are both in the 'SFG' part of the classification.

6 DISCUSSION

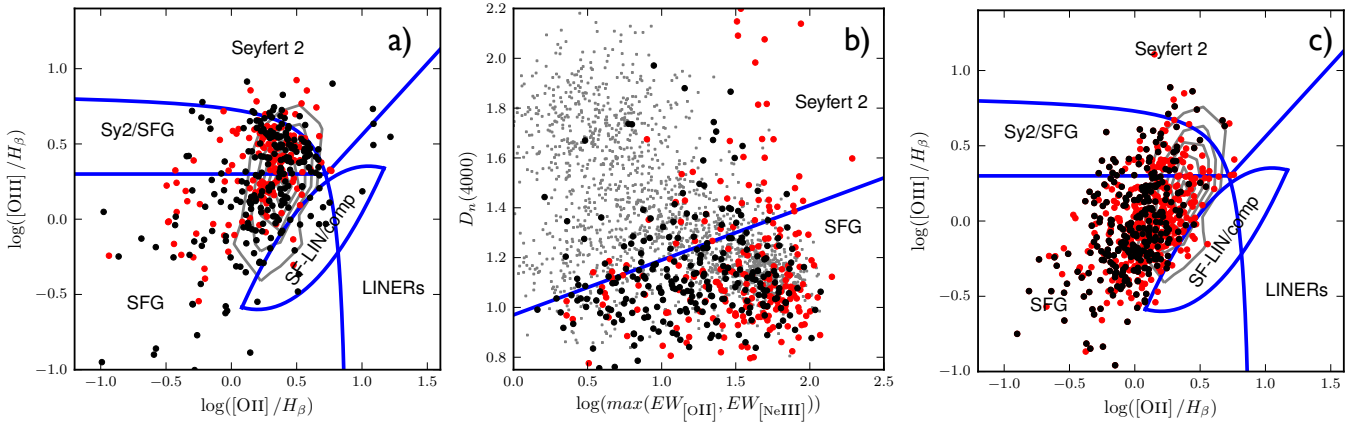
6.1 Redshift identification rates in *ugr* and *gri*

We summarize the redshift measurement efficiency of the *gri* and *ugr* colour-selected galaxies presented in this paper in Tables 3 and 5, and we compare the results with those of WiggleZ (Drinkwater et al. 2010), BOSS and VIPERS (the percentages about VIPERS are based on a preliminary subset including only ~ 20 percent of the survey). The original VIPERS selection flag (J. Coupon and O. Ilbert private communication) is defined to have colours compatible with an object at $z > 0.5$ if it has $(r-i \geq 0.7 \text{ and } u-g \geq 1.4)$ or $(r-i \geq 0.5(u-g) \text{ and } u-g < 1.4)$ (Guzzo et al. (2012), in preparation). The efficiencies in the Table 5 show that a better photometry and thus more precise colours yield a better efficiency in terms of obtaining objects in the targeted redshift range. It also shows the colour selections proposed in this paper are competitive for building an LSS sample.

To determine the necessary precision on the photometry to stay at the efficiencies observed, we degrade the photometry of the observed ELGs, then reselect them and recompute the efficiencies. Using a photometry less precise than the CFHTLS by a factor of 2.5

Table 4. Main properties of the observed galaxies. Fluxes are in unit of 10^{-17} erg cm $^{-2}$ s $^{-1}$. Equivalent Widths ‘EW’ are in Å.

	<i>gri</i> -selected ELG				<i>ugr</i> -selected ELG			
	CFHTLS		SDSS		CFHTLS		SDSS	
	mean	σ	mean	σ	mean	σ	mean	σ
EW _[OII]	-14.86	9.01	-16.75	10.13	-50.58	27.24	-30.75	23.04
Flux _[OII]	16.85	9.65	18.58	10.37	30.36	30.1	24.23	39.27
EW _{Hβ}	-10.28	10.8	-10.72	8.65	-24.27	22.88	-17.18	19.34
Flux _{Hβ}	15.44	8.6	14.63	7.72	12.97	15.16	12.57	23.91
EW _[OIII]	-10.09	10.98	-11.33	10.76	-65.3	91.56	-16.89	30.49
Flux _[OIII]	17.74	20.15	17.43	21.59	35.13	53.49	13.39	37.79
12 + log <i>OH</i>	8.94	0.20	8.92	0.19	8.69	0.21	8.69	0.25
logSFR _[OII]	0.97	0.35	0.92	0.45	0.96	1.24	0.76	0.84
log(<i>M</i> [*] / <i>M</i> _⊙)	10.85	0.3	10.23	6.87	9.33	0.80	-	-

**Figure 9.** Black dots stands for CFHTLS selected ELGs, red dots for SDSS selected ELGs and grey contours or grey pixels for zCOSMOS survey galaxies. **a)** $\log([OII]/H\beta)$ vs. $\log([OIII]/H\beta)$ for *ugr* ELGs. The *ugr* ELG sample is located in a similar area than zCOSMOS galaxies. **b)** $D_n(4000)$ vs. $\log(\max(EW_{[OII]}, EW_{[NeIII]}))$ for *ugr* ELGs. Only galaxies from the ‘Sy2/SFG’ area from the plot a) are represented. The *ugr* ELG is thus mainly composed of ‘SFG’. **c)** $\log([OII]/H\beta)$ vs. $\log([OIII]/H\beta)$ for *gri* ELGs. The *gri* ELG sample is located in the ‘SFG’ area.

in the errors (the ratio of the median values of the mag errors in bins of 0.1 in magnitude equals 2.5) does not significantly change neither the efficiency nor the redshift distribution implied by the colour selection. This change also corresponds to loosening the colour criterion by 0.1 mag. For the *eBOSS* survey a photometry 2.5 times less precise than CFHTLS should be sufficient to maintain a high targeting efficiency (for comparison, SDSS is 10 times less precise than CFHTLS); Fig. 10 shows the smearing of the galaxy positions in the colour-colour plane for a degraded photometry.

6.2 Measurement of the [OII] doublet, single emission line spectra

For ground-based spectroscopic surveys observing ELGs with $1 < z < 1.7$, the only emission line remaining in the spectrum to assign the spectroscopic redshift is the [OII] doublet. For the redshift to be certain the doublet must be split (*i.e.*, we do not want the target to be classified as ‘single emission line’ ELG). Fig. 11 shows a subsample of the observed bright *ugr* ELGs where [OII] doublets are well resolved.

We can circumvent the ‘single emission line’ ELG issue (Fig. 6) by increasing the resolution of the spectrograph. This modification will enhance a better split of [OII], and will increase the room

Table 5. Redshift efficiency in percent. The second column ‘spectroscopic redshift’ quantifies the amount of spectroscopic redshift obtained with the selection. The third column ‘object in *z* window’ is the number of spectroscopic redshift that are in the range the survey is aiming at, it is the efficiency of the target selection. The redshift window for ELG selection is $z > 0.6$.

selection scheme	spectroscopic redshift	object in <i>z</i> window	quasars
<i>gri</i> SDSS	80	62	1
<i>gri</i> CFHTLS	82	73	1
<i>ugr</i> SDSS	80	32	10
<i>ugr</i> CFHTLS	78	56	13
WiggleZ	60	35	-
BOSS	95	95	-
VIPERS	80	70	-

available to observe the doublet by rendering sky lines ‘thinner’. The sky acts as an observational window and prevents some narrow redshift ranges to be sampled by the spectrograph; see Fig. 8. Increasing the resolution dilutes the signal, and thus the exposure time has to be increased to reconstruct properly the doublet above the mean sky level.

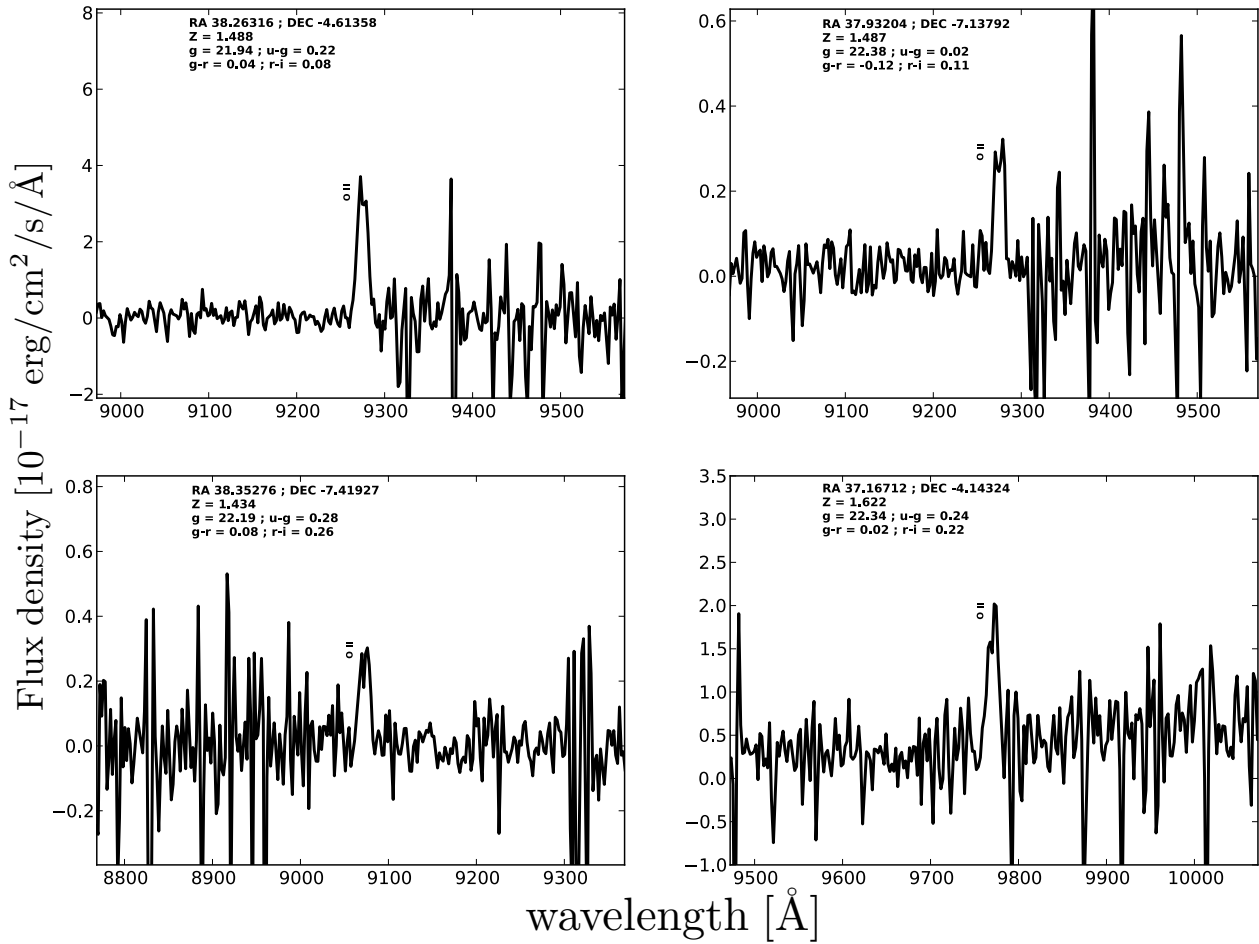


Figure 11. Observed Spectra zoomed on the [OII] doublet, extracted from the *ugr* ELG sample. The doublet is enough split (apart from a little blending) to assign the correct spectroscopic redshift without the help of other emission lines.

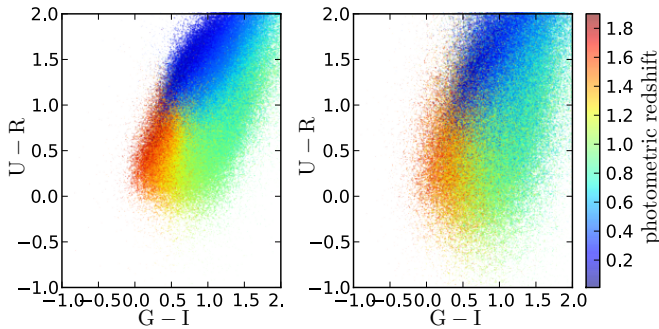


Figure 10. U-R vs. G-I colored according to the photometric redshift. On the left CFHT-LS photometry, on the right CFHT-LS photometry degraded by a factor 2.5. This comparison shows how the degradation of the photometry smears the clean separations between galaxy populations in redshift.

We performed a simulation of the [OII] emission line fit to quantify by which amount the resolution must be increased to have no ‘single emission line’ ELGs. We fit one or two Gaussians on a doublet with a total flux of $10^{-16} \text{erg s}^{-1} \text{cm}^{-2}$ (lowest

‘single emission line’ flux observed) contaminated by a noise of $3 \times 10^{-17} \text{erg s}^{-1} \text{cm}^{-2}$ (typical BOSS dark sky). The χ^2 of the two fits are equal at low resolution and become disjoint in favor of the fit with 2 Gaussians for a resolution above 3000 at 7454.2 Å (*i.e.* [OII] at redshift 1). Such an increase in resolution could help assigning proper redshifts to ‘single emission line’ ELGs.

6.3 How / why redshift went wrong

The main difference in redshift measurement efficiency between SDSS and CFHT-LS colour selection is mainly due to the difference in photometry depth. Using calibrations made by Regnault et al. (2009), it is possible to translate the colour selection criteria from CFHT-LS magnitudes to SDSS magnitudes. The colour difference can be as large as 1 magnitude as the SDSS magnitude cut is close to the detection limit of the SDSS survey; see Fig. 12 where SDSS *gri* colour-selected galaxies are represented with their CFHTLS magnitudes.

6.4 How to improve ELG selection for future surveys

We suggest a few ways to increase the redshift measurement efficiency and reach the requirements set in the second section.

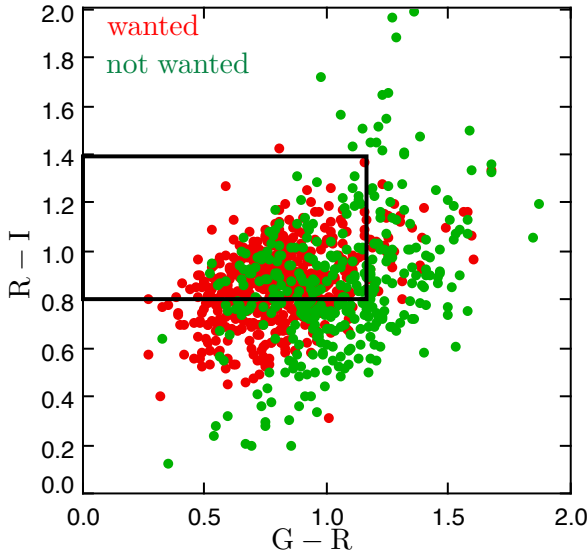


Figure 12. *gri* selection based on colours from SDSS (black box) represented on CFHTLS magnitudes. The scatter is quite large: about half the targets would not have been selected if we used CFHTLS photometry. The ‘wanted’ objects are galaxies at $z > 0.6$ or quasars and ‘unwanted’ objects are the rest.

For the *ugr* selection : lowering *u-g* cut to 0.3 diminishes the contamination by low-redshifts galaxies. Additional low-redshift galaxies can be removed from the selection through an inspection of the images. Some of the low-redshift galaxies are quite extended, and one could mistake a high-redshift merger for an extended low-redshift galaxy. Visual inspection reduces the low-redshift share from 9 percent to 4 percent. The compact and extended selection on the CFHT data is very efficient at identifying quasars. There is also room for improving the spectroscopic redshift determination and thus re-classify ‘single emission line’ galaxies : they represent a 12 percent share, among which 10 percent are at $z > 0.6$. It seems reasonable to assume an efficiency improvement from 46 percent $\text{ELG}(z > 0.6)$ + 14 percent quasar to 61 percent $\text{ELG}(z > 0.6)$ + 14 percent quasar. Thus a total efficiency of $\sim 75\%$

For the *gri* selection : improving the spectroscopic redshift determination pipeline can gain up to 5 percent efficiency thus increasing from 73 to 78 percent of $\text{ELG}(z > 0.6)$.

We have also optimized target selections for BAO sampling density using the four bands *ugri*. We find that the optimum selections have a redshift distribution close to the smooth combination of the *gri* and *ugr* selections discussed here; see Fig. 13.

7 CONCLUSION

We present an efficient emission-line galaxy selection that can provide a sample from which one can measure the BAO feature in the 2-point correlation function at $z > 0.6$. With the photometry available today we can plan for a BAO measure to redshift 1 with the BOSS spectrograph.

A representative set of photometric surveys that might be available for target selection in a near future on more than 2,000 square degrees are :

- The Kilo Degree Survey (KIDS)¹¹ aims at observing 1500 square degrees in the *ugri* bands with 3σ depth of 24.8, 25.4, 25.2, 24.2 using the VST.
- the South Galactic Cap U-band Sky Survey¹² (SCUSS) aims a 5σ limiting magnitude of 23.0
- the Dark Energy Survey (DES) aims at observing 5,000 square degrees in *griz* bands with 10σ depth of 24.6, 24.1, 24.3, 23.9. This survey does not include the *u* band (The Dark Energy Survey Collaboration 2005; Banerji et al. 2008).
- the Large Synoptic Survey Telescope (LSST) (Ivezic et al. 2008) plans to observe 20,000 square degrees in *ugrizy* bands with 5σ depth of 26.1, 27.4, 27.5, 26.8, 26.1, 24.9.

Using such deeper photometric surveys and improved pipelines, it should be possible to probe BAO to redshift $z = 1.2$ in the next 6 years, *e.g.* by the *eBOSS* experiment, and to $z = 1.7$ in the next 10 years, *e.g.* by PFS-SuMIREor *BigBOSS* experiment.

ACKNOWLEDGEMENTS

Johan Comparat especially thanks Carlo Schmid and Olivier Ilbert for insightful discussions about this observational program and its interpretation.

We thank the SDSS-III/BOSS collaboration for granting us this ancillary program.

Funding for SDSS-III has been provided by the Alfred P. Sloan Foundation, the Participating Institutions, the National Science Foundation, and the U.S. Department of Energy Office of Science. The SDSS-III web site is <http://www.sdss3.org/>.

SDSS-III is managed by the Astrophysical Research Consortium for the Participating Institutions of the SDSS-III Collaboration including the University of Arizona, the Brazilian Participation Group, Brookhaven National Laboratory, University of Cambridge, Carnegie Mellon University, University of Florida, the French Participation Group, the German Participation Group, Harvard University, the Instituto de Astrofísica de Canarias, the Michigan State/Notre Dame/JINA Participation Group, Johns Hopkins University, Lawrence Berkeley National Laboratory, Max Planck Institute for Astrophysics, Max Planck Institute for Extraterrestrial Physics, New Mexico State University, New York University, Ohio State University, Pennsylvania State University, University of Portsmouth, Princeton University, the Spanish Participation Group, University of Tokyo, University of Utah, Vanderbilt University, University of Virginia, University of Washington, and Yale University.

Based on observations obtained with MegaPrime/MegaCam, a joint project of CFHT and CEA/DAPNIA, at the Canada-France-Hawaii Telescope (CFHT) which is operated by the National Research Council (NRC) of Canada, the Institut National des Sciences de l’Univers of the Centre National de la Recherche Scientifique (CNRS) of France, and the University of Hawaii. This work is based in part on data products produced at TERAPIX and the Canadian Astronomy Data Centre as part of the Canada-France-Hawaii Telescope Legacy Survey, a collaborative project of NRC and CNRS.

The BOSS French Participation Group is supported by Agence Nationale de la Recherche under grant ANR-08-BLAN-0222.

¹¹ <http://kids.strw.leidenuniv.nl/>

¹² <http://batc.bao.ac.cn/Uband/>

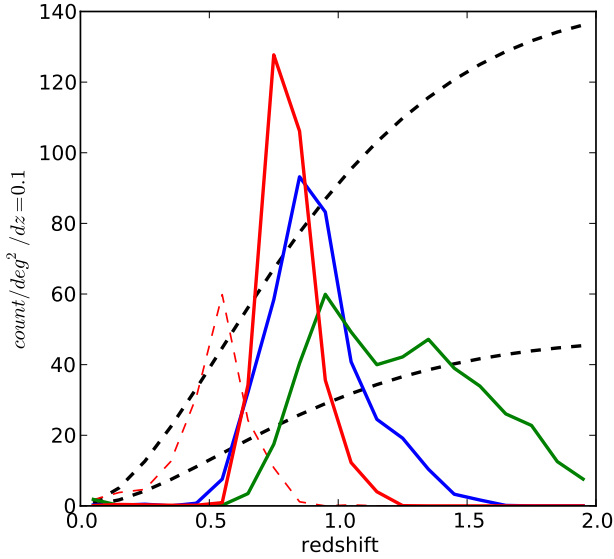


Figure 13. Photometric redshift distributions obtained using the *ugri* bands. The dashed black lines are the low and high density goals mentioned in Section 2, $\bar{n} = 10^{-4}$ and $3 \times 10^{-4} h^3 \text{Mpc}^{-3}$. The dashed red line is the BOSS CMASS sample. The solid blue line is the distribution enhanced by the *ugri* selection, it has a projected sky density of $\sim 340 \text{ deg}^{-2}$. The solid red line is the *gri* selection (projected sky density $\sim 350 \text{ deg}^{-2}$). The solid green is the *ugr* selection (projected sky density $\sim 400 \text{ deg}^{-2}$). It shows the possibility of making a selection able to sample [0.6, 1.2] for a BAO experiment.

References

Abazajian K. N. et al., 2009, *ApJS*, 182, 543
 Abraham R. G., Tanvir N. R., Santiago B. X., Ellis R. S., Glazebrook K., van den Bergh S., 1996, *MNRAS*, 279, L47
 Adelberger K. L., Steidel C. C., Shapley A. E., Hunt M. P., Erb D. K., Reddy N. A., Pettini M., 2004, *Astrophys. J.*, 607, 226
 Aihara H. et al., 2011, *ApJS*, 193, 29
 Anderson L. et al., 2012, ArXiv e-prints: 1203.6594
 Argence B., Lamareille F., 2009, *A&A*, 495, 759
 Astier P. et al., 2006, *A&A*, 447, 31
 Banerji M., Abdalla F. B., Lahav O., Lin H., 2008, *MNRAS*, 386, 1219
 Blake C., Glazebrook K., 2003, *Astrophys. J.*, 594, 665
 Blake C. et al., 2011, *MNRAS*, 418, 1707
 Bovy J. et al., 2011, *Astrophys. J.*, 729, 141
 Brinchmann J., Charlot S., White S. D. M., Tremonti C., Kauffmann G., Heckman T., Brinkmann J., 2004, *MNRAS*, 351, 1151
 Bruzual G., Charlot S., 2003, *MNRAS*, 344, 1000
 Cannon R. et al., 2006, *MNRAS*, 372, 425
 Capak P. et al., 2007, *ApJS*, 172, 99
 Coil A. L. et al., 2008, *Astrophys. J.*, 672, 153
 Cole S. et al., 2005, *MNRAS*, 362, 505
 Cooper M. C. et al., 2008, *MNRAS*, 383, 1058
 Coupon J. et al., 2009, *A&A*, 500, 981
 Davis M. et al., 2003, in Presented at the Society of Photo-Optical Instrumentation Engineers (SPIE) Conference, Vol. 4834, Society of Photo-Optical Instrumentation Engineers (SPIE) Conference Series, P. Guhathakurta, ed., pp. 161–172
 Dawson K. S. et al., 2009, *AJ*, 138, 1271

Dickinson M., Papovich C., Ferguson H. C., Budavári T., 2003, *Astrophys. J.*, 587, 25
 Drinkwater M. J. et al., 2010, *MNRAS*, 401, 1429
 Eisenstein D. J. et al., 2001, *AJ*, 122, 2267
 Eisenstein D. J., Seo H.-J., Sirko E., Spergel D. N., 2007a, *Astrophys. J.*, 664, 675
 Eisenstein D. J., Seo H.-J., White M., 2007b, *Astrophys. J.*, 664, 660
 Eisenstein D. J. et al., 2011, *AJ*, 142, 72
 Eisenstein D. J. et al., 2005, *Astrophys. J.*, 633, 560
 Fukugita M., Ichikawa T., Gunn J. E., Doi M., Shimasaku K., Schneider D. P., 1996, *AJ*, 111, 1748
 Garilli B. et al., 2008, *A&A*, 486, 683
 Gunn J. E. et al., 1998, *AJ*, 116, 3040
 Gunn J. E. et al., 2006, *AJ*, 131, 2332
 Ilbert O. et al., 2006, *A&A*, 457, 841
 Ilbert O. et al., 2009, *Astrophys. J.*, 690, 1236
 Ivezić Z. et al., 2008, ArXiv e-prints: 0805.2366
 Jouvel S. et al., 2009, *A&A*, 504, 359
 Kaiser N., 1986, *MNRAS*, 219, 785
 Kennicutt, Jr. R., 1998, *Annual Review of A&A*, 36, 189
 Komatsu E. et al., 2009, *ApJS*, 180, 330
 Komatsu E. et al., 2011, *ApJS*, 192, 18
 Lamareille F., 2010, *A&A*, 509, A53+
 Lamareille F. et al., 2009, *A&A*, 495, 53
 Lamareille F., Contini T., Brinchmann J., Le Borgne J.-F., Charlot S., Richard J., 2006, *A&A*, 448, 907
 Le Fèvre O. et al., 2005a, *Nature*, 437, 519
 Le Fèvre O. et al., 2005b, *A&A*, 439, 845
 Lilly S. J. et al., 2009, *ApJS*, 184, 218
 Marocco J., Hache E., Lamareille F., 2011, *A&A*, 531, A71
 Martin D. C. et al., 2005, *ApJ*, 619, L1
 Padmanabhan N., Xu X., Eisenstein D. J., Scalzo R., Cuesta A. J., Mehta K. T., Kazin E., 2012, ArXiv e-prints: 1202.0090
 Peebles P. J. E., Yu J. T., 1970, *Astrophys. J.*, 162, 815
 Percival W. J. et al., 2010, *MNRAS*, 401, 2148
 Perlmuter S. et al., 1999, *Astrophys. J.*, 517, 565
 Regnault N. et al., 2009, *A&A*, 506, 999
 Riess A. G. et al., 1998, *AJ*, 116, 1009
 Riess A. G. et al., 2011, *Astrophys. J.*, 730, 119
 Riess A. G. et al., 2007, *Astrophys. J.*, 659, 98
 Riess A. G. et al., 2004, *Astrophys. J.*, 607, 665
 Schlegel D. et al., 2011, ArXiv e-prints: 1106.1706
 Schlegel D. J., Finkbeiner D. P., Davis M., 1998, *Astrophys. J.*, 500, 525
 Scoville N. et al., 2007, *ApJS*, 172, 1
 Tegmark M., 1997a, *Physical Review Letters*, 79, 3806
 Tegmark M., 1997b, *Physical Review Letters*, 79, 3806
 The Dark Energy Survey Collaboration, 2005, ArXiv e-prints: 0510.346
 Thomas D. et al., 2012, ArXiv e-prints
 Tremonti C. A. et al., 2004a, *Astrophys. J.*, 613, 898
 Tremonti C. A. et al., 2004b, *Astrophys. J.*, 613, 898
 Wood-Vasey W. M. et al., 2007, *Astrophys. J.*, 666, 694
 Zhu G., Moustakas J., Blanton M. R., 2009, *Astrophys. J.*, 701, 86

Table A1. 43 ELGs from the *gri* selection and their observed properties. The error on the redshift determined by the software is not yet fully reliable and thus not displayed. The complete ELG dataset will be included in SDSS Data Release 9 in July 2012.

RA (J2000)	DEC (J2000)	redshift	g	r	i	r_2	r_2^{limit}	$\log M_*$	$EW^{3727}_{[OII]}$	$flux^{3727}_{[OII]}$	$EW^{5007}_{[OII]}$	$flux^{5007}_{[OII]}$	D_{4n}	$12\log(O/H)$	$\log(SFR_{H\beta})$	$\log(SFR_{[OII]})$
213.6918335	52.7059669	0.6055	22.79	22.13	21.28	3.46	2.4	10.5	-15.0	14.15	-3.98	4.57	1.12	8.77	0.35	0.68
214.8627014	51.775528	0.6057	22.96	21.87	20.85	3.16	3.04	10.55	-4.1	6.5	-3.06	5.37	1.21	9.05	0.61	0.18
214.234848	53.0964775	0.6074	23.0	22.29	21.18	4.16	2.69	10.35	-13.97	12.06	-5.67	4.43	1.45	8.65	0.39	0.58
213.7070465	52.2989693	0.6169	22.2	21.52	20.65	5.11	2.62	10.52	-6.95	7.76	-11.71	18.04	1.27	9.0	0.76	0.31
216.1340179	53.6467667	0.6216	22.62	21.72	20.79	4.03	2.63	10.67	-14.3	20.84	-8.74	9.13	1.11	8.92	0.83	0.96
213.3887024	53.5097351	0.6233	21.97	21.3	20.28	5.98	2.16	10.98	-17.69	19.41	-1.75	3.02	1.15	9.19	1.26	0.91
215.3585205	52.8954582	0.6319	22.71	22.06	21.24	4.2	2.85	10.41	-6.48	5.94	-5.89	5.49	1.05	9.09	0.54	0.17
213.268158	53.4914665	0.6325	22.79	21.73	20.71	3.06	2.16	10.83	-3.63	3.33	-2.96	5.85	1.21	9.07	0.39	-0.21
216.0396729	53.8974152	0.6453	22.17	21.39	20.52	3.75	2.63	10.72	-13.94	15.13	-10.69	19.87	1.25	8.86	0.85	0.79
213.7992401	53.8096962	0.6486	22.78	21.81	20.78	3.96	2.69	10.62	-10.3	10.82	-9.41	12.07	1.26	9.03	0.8	0.58
213.3646545	52.2972374	0.6516	22.55	21.97	20.8	5.33	2.4	10.65	-6.27	8.9	-8.67	9.83	1.05	8.89	0.48	0.46
214.332962	52.1850281	0.6713	22.92	22.1	21.13	3.39	3.04	10.58	-5.77	6.99	-11.25	19.21	1.35	8.73	0.69	0.34
215.8718262	52.804966	0.6728	22.86	21.97	21.06	4.51	2.85	10.39	-22.57	18.81	-14.13	14.35	1.38	8.61	0.64	0.98
216.0170441	53.2218399	0.6745	22.73	21.77	20.74	4.43	2.63	10.67	-6.25	6.94	-9.26	13.23	1.32	8.79	0.42	0.34
213.0988007	53.3722191	0.7115	22.2	21.58	20.63	3.56	2.16	10.83	-6.5	10.66	-5.93	10.26	1.44	8.95	0.84	0.67
213.3162994	52.2124023	0.7172	22.38	22.12	21.16	4.59	2.4	10.09	-28.72	23.85	-17.58	14.36	1.31	8.86	0.95	1.2
216.207016	53.3441353	0.7214	22.68	21.65	20.75	6.29	2.63	10.91	-5.67	7.19	-12.6	21.03	1.33	8.93	0.92	0.43
215.2261353	54.4270706	0.7232	22.51	21.75	20.84	4.74	2.77	10.91	-15.3	23.72	-15.91	29.68	1.33	8.98	1.22	1.2
214.0466309	54.2588539	0.7332	22.58	21.85	20.88	3.56	2.94	10.34	-15.25	12.34	-14.08	18.21	1.05	9.1	1.2	0.8
216.872467	53.8220406	0.7384	22.32	21.76	20.84	4.64	2.69	11.05	-8.17	8.28	-6.1	11.15	1.27	9.07	1.19	0.55
215.8093567	52.568676	0.7435	22.07	21.24	20.22	3.54	2.85	11.07	-8.75	12.48	-10.71	25.15	1.29	8.75	0.87	0.82
214.6755829	52.3814735	0.7474	22.72	21.87	20.91	3.66	2.62	10.78	-37.32	41.68	-4.67	11.07	1.19	8.87	1.09	1.6
214.9938507	53.0233078	0.7536	22.37	21.57	20.54	3.85	2.62	11.15	-10.54	10.98	-3.2	5.18	1.28	9.18	1.15	0.75
216.4916077	52.4496536	0.7655	22.24	21.59	20.64	4.69	2.85	11.01	-5.49	8.42	-3.18	5.86	1.38	9.04	0.72	0.59
215.0812225	54.1586342	0.7663	22.58	22.17	21.1	3.44	2.94	10.56	-11.64	16.8	-6.87	9.62	1.13	8.9	1.06	1.04
213.9476013	52.7977905	0.7667	22.56	21.56	20.34	3.31	2.62	10.84	-1.5	1.94	-2.29	4.6	1.38	9.09	0.8	-0.35
214.9521484	53.7672997	0.7691	22.91	21.95	20.86	3.44	2.69	10.7	-8.77	11.81	-2.11	3.95	1.36	8.59	0.48	0.82
215.9055939	53.82481	0.7727	21.84	20.94	19.96	7.69	2.63	10.75	-22.57	16.87	-6.3	8.81	1.18	8.91	0.91	1.05
213.0868225	53.8581505	0.7814	22.47	21.93	21.09	5.33	2.16	10.65	-26.32	18.35	-20.79	12.91	1.22	8.76	0.92	1.12
214.3099976	53.5430412	0.7861	22.19	21.75	20.93	5.76	2.69	10.54	-10.87	9.3	-5.97	9.67	1.1	9.1	1.14	0.69
215.021637	53.6823692	0.7931	22.99	22.1	21.27	4.73	2.69	10.6	-16.75	16.98	-8.86	11.09	1.65	8.69	0.88	1.08
215.9687347	51.9373779	0.7978	22.12	21.13	20.11	6.64	2.68	10.8	-16.96	17.64	-7.46	13.64	1.62	9.15	1.69	1.11
217.0994263	53.6485252	0.8021	22.81	22.11	20.94	3.66	2.69	11.27	-12.05	12.49	-4.75	12.7	1.4	9.06	1.33	0.9
216.3505859	52.7362518	0.8079	22.44	21.62	20.58	4.16	2.85	11.05	-6.42	8.53	-7.3	14.12	1.3	9.01	0.93	0.66
215.0271912	54.4110947	0.8181	21.54	20.96	20.09	7.11	2.94	11.16	-5.9	11.1	-8.92	22.59	1.47	8.94	1.03	0.84
216.8689117	53.2321129	0.8214	22.0	21.31	20.32	4.8	2.69	10.93	-11.2	10.4	-6.9	7.24	1.41	8.85	0.59	0.8
215.1800842	54.4046021	0.8464	22.43	21.51	20.24	4.92	2.94	11.09	-7.72	8.44	-13.94	26.07	1.25	8.91	1.11	0.7
216.5852509	52.9398422	0.8488	22.39	21.55	20.67	3.1	2.85	11.09	-22.16	27.22	-5.64	12.9	1.43	9.03	1.37	1.46
215.3106842	53.2784233	0.8642	22.59	22.04	20.8	5.19	2.63	10.72	-7.99	10.51	-5.91	11.28	1.26	8.64	0.51	0.86
212.5664368	53.6004372	0.9565	22.41	22.02	21.11	3.21	2.16	10.77	-19.32	30.01	-25.59	54.22	1.33	8.75	1.54	1.64
216.5693207	52.5144348	0.9634	22.84	22.2	21.27	4.66	2.85	10.23	-33.12	52.26	-58.21	109.58	1.24	8.67	1.73	2.0
215.3971405	54.5257492	0.9755	22.13	21.83	20.94	3.32	2.77	10.2	-28.61	41.02	-27.8	58.98	1.19	8.85	1.59	1.86
214.368927	53.5621452	1.191	22.7	22.17	20.85	2.27	2.69	11.75	-9.52	24.57	0.0	0.0	1.55	-Infinity	-Infinity	1.72

Figure A1. *ugr*-selected ELGs at $z < 0.5$. The spectra are represented in f_λ convention. The coloured image on the left is courtesy of CFHT cutout service. The black and white image in the center is the *g*-band. The observed object is the one in the centre of the images.

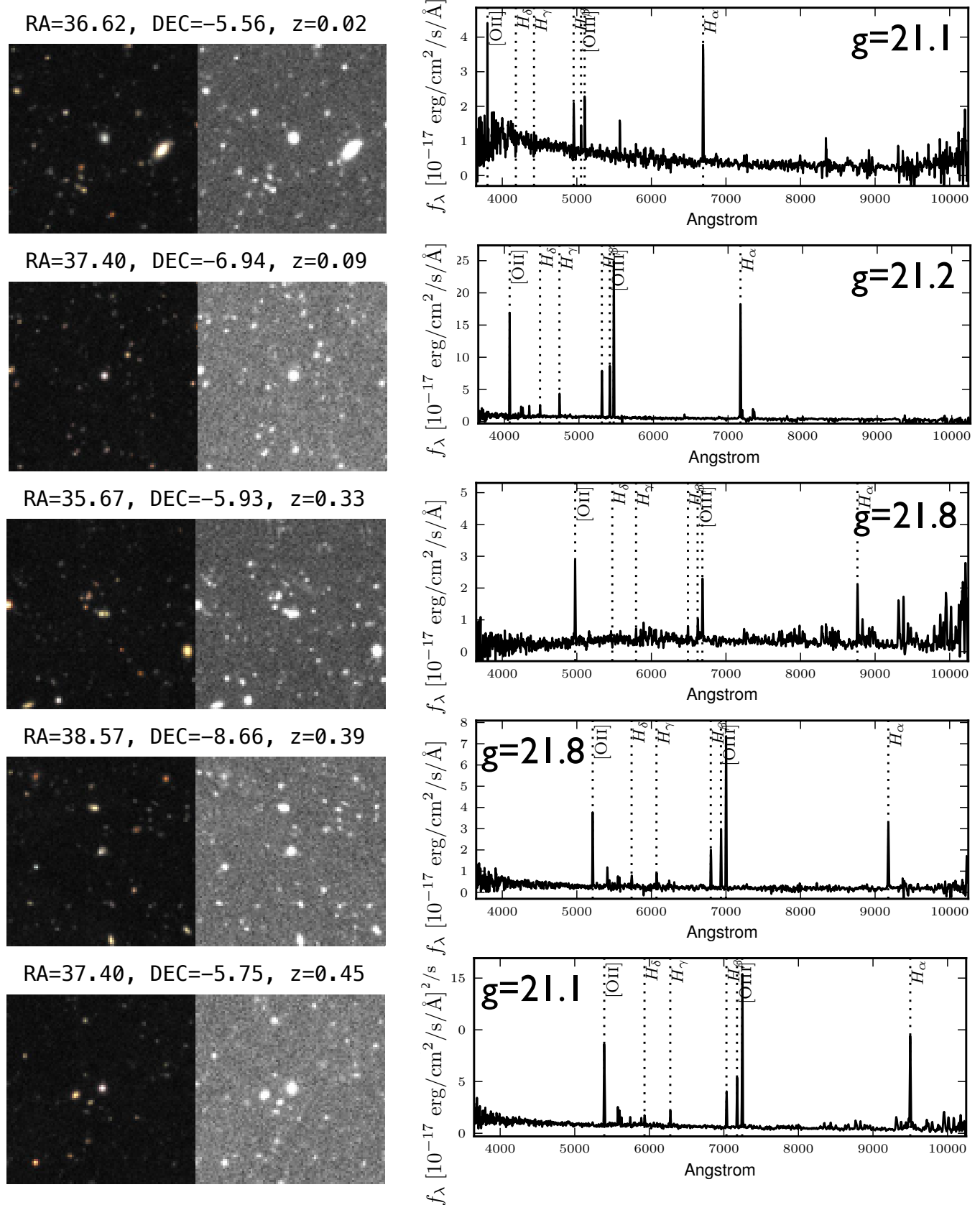


Figure A2. *ugr*-selected ELGs at $0.5 < z < 1.0$. The spectra are represented in f_λ convention. The coloured image on the left is courtesy of CFHT cutout service. The black and white image in the center is the *g*-band. The observed object is the one in the centre of the images.

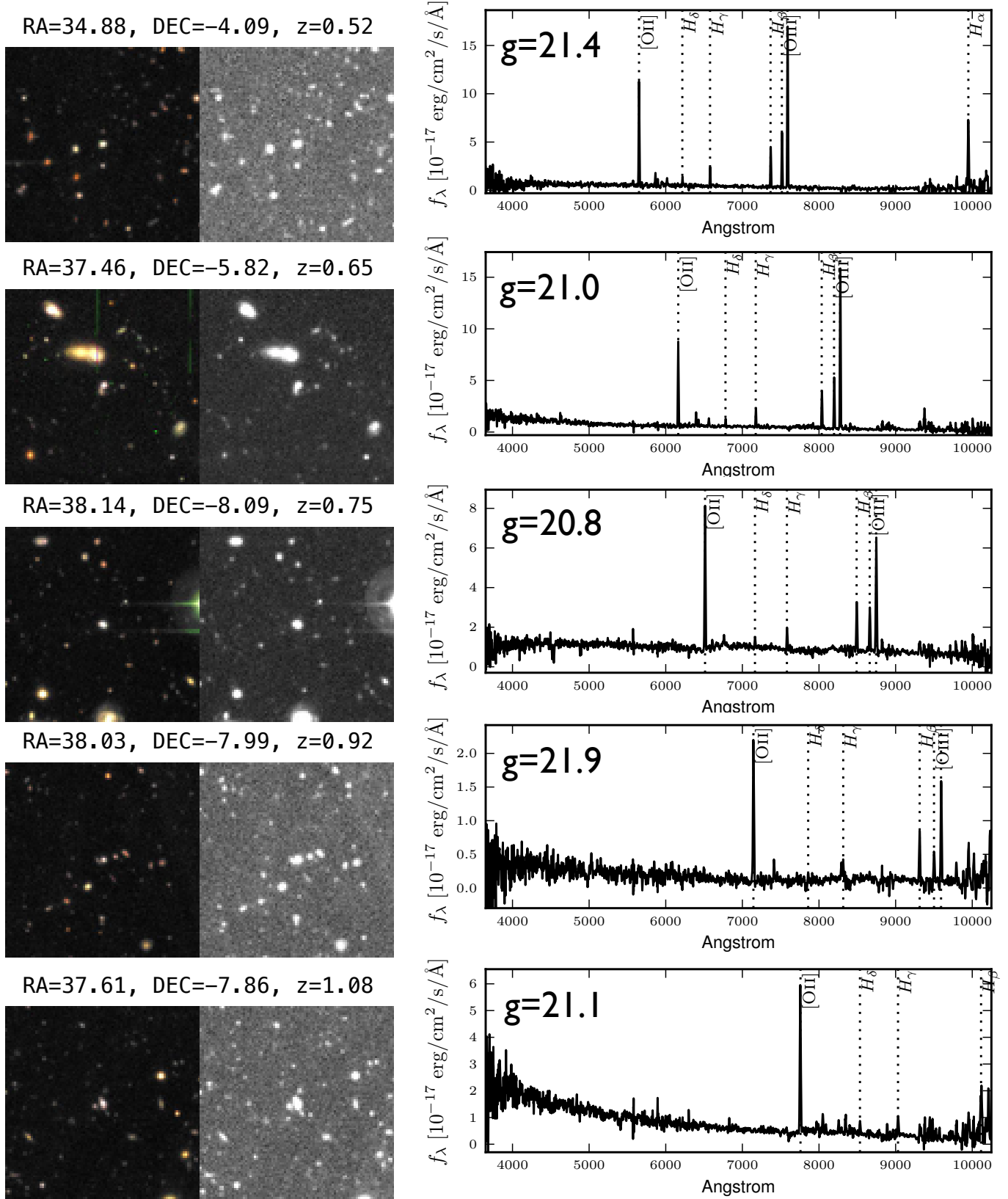


Figure A3. *ugr*-selected ELGs at $1.0 < z < 1.6$. The spectra are represented in f_λ convention. The coloured image on the left is courtesy of CFHT cutout service. The black and white image in the center is the *g*-band. The observed object is the one in the centre of the images.

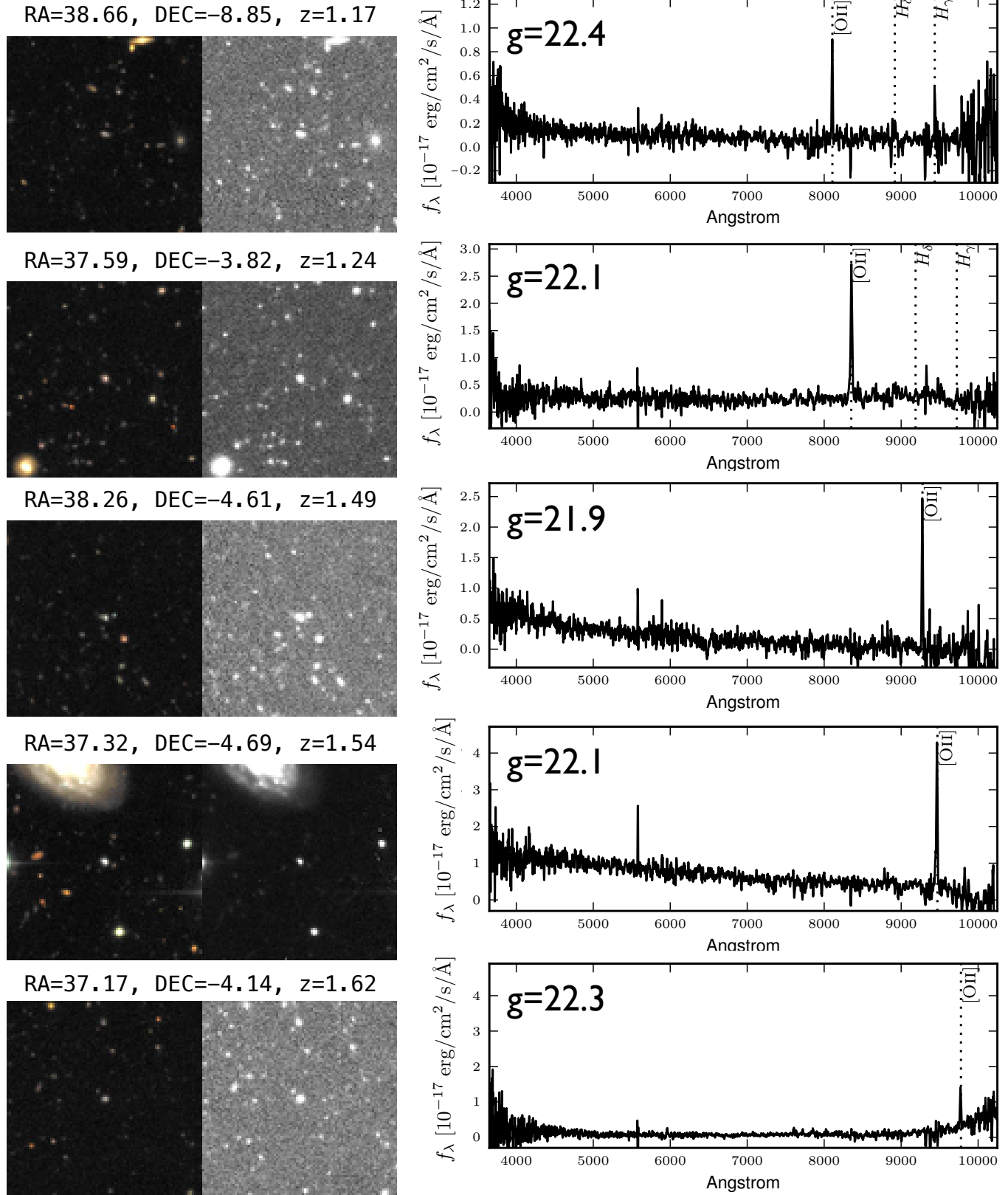


Figure A4. *ugr*-selected quasars at $1.0 < z < 2.3$. The spectra are represented in f_λ convention. The coloured image on the left is courtesy of CFHT cutout service. The black and white image in the center is the *g*-band. The observed object is the one in the centre of the images.

